Bioactive Materials 37 (2024) 222–238

Contents lists available at ScienceDirect

Bioactive Materials

journal homepage: www.keaipublishing.com/en/journals/bioactive-materials

ETV2 regulating PHD2-HIF-1α axis controls metabolism reprogramming promotes vascularized bone regeneration

HaoRan Du [a,b,1], Bang Li [a,1], Rui Yu [a,1], Xiaoxuan Lu [a], ChengLin Li [a], HuiHui Zhang [a], Fan Yang [a], RongQuan Zhao [a], WeiMin Bao [a], Xuan Yin [a], YuanYin Wang [a,***], Jian Zhou [b,c,d,**], Jianguang Xu [a,*]

[a] College & Hospital of Stomatology, Anhui Medical University, Key Lab. of Oral Diseases Research of Anhui Province, Hefei, 230032, China
[b] Salivary Gland Disease Center and Beijing Key Laboratory of Tooth Regeneration and Function Reconstruction, Beijing Laboratory of Oral Health and Beijing Stomatological Hospital, Capital Medical University, Beijing, 100050, China
[c] Department of VIP Dental Service, School of Stomatology, Capital Medical University, Beijing, 100050, China
[d] Laboratory for Oral and General Health Integration and Translation, Beijing Tiantan Hospital, Capital Medical University, Beijing, China

ARTICLE INFO

Keywords:
Vascularized bone regeneration
ETV2
Hypoxia-inducible factor-1α
Metabolism reprogramming
Microsphere

ABSTRACT

The synchronized development of mineralized bone and blood vessels is a fundamental requirement for successful bone tissue regeneration. Adequate energy production forms the cornerstone supporting new bone formation. ETS variant 2 (ETV2) has been identified as a transcription factor that promotes energy metabolism reprogramming and facilitates the coordination between osteogenesis and angiogenesis. In vitro molecular experiments have demonstrated that ETV2 enhances osteogenic differentiation of dental pulp stem cells (DPSCs) by regulating the ETV2- prolyl hydroxylase 2 (PHD2)- hypoxia-inducible factor-1α (HIF-1α)- vascular endothelial growth factor A (VEGFA) axis. Notably, ETV2 achieves the rapid reprogramming of energy metabolism by simultaneously accelerating mitochondrial aerobic respiration and glycolysis, thus fulfilling the energy requirements essential to expedite osteogenic differentiation. Furthermore, decreased α-ketoglutarate release from ETV2-modified DPSCs contributes to microcirculation reconstruction. Additionally, we engineered hydroxyapatite/chitosan microspheres (HA/CS MS) with biomimetic nanostructures to facilitate multiple ETV2-DPSC functions and further enhanced the osteogenic differentiation. Animal experiments have validated the synergistic effect of ETV2-modified DPSCs and HA/CS MS in promoting the critical-size bone defect regeneration. In summary, this study offers a novel treatment approach for vascularized bone tissue regeneration that relies on energy metabolism activation and the maintenance of a stable local hypoxia signaling state.

1. Introduction

The regeneration of bone defects arising from trauma, infection, tumor resection, and skeletal abnormalities remains a significant challenge in maxillofacial surgery [1]. The use of diverse bone substitutes for grafting has become increasingly common, with over 2 million procedures conducted globally each year [2]. However, limited progenitor cell differentiation and the occurrence of avascular necrosis, often attributes to inadequate vascularization and can lead to delayed healing and nonunion [3,4]. In large bone defect studies involving animal models, a multitude of scaffolds exhibit restricted bone-healing capabilities owing to their low osteogenic induction activity and inadequate vascularization. This limitation has impeded their clinical

Peer review under responsibility of KeAi Communications Co., Ltd.

* Corresponding author. College & Hospital of Stomatology, Anhui Medical University, Key Lab. of Oral Diseases Research of Anhui Province, Hefei, 230032, China.

** Corresponding author. Salivary Gland Disease Center and Beijing Key Laboratory of Tooth Regeneration and Function Reconstruction, Beijing Laboratory of Oral Health and Beijing Stomatological Hospital, Capital Medical University, Beijing, 100050, China.

*** Corresponding author. College & Hospital of Stomatology, Anhui Medical University, Key Lab. of Oral Diseases Research of Anhui Province, Hefei, 230032, China.

E-mail addresses: wyy1970548@sohu.com (Y. Wang), zhoujian@ccmu.edu.cn (J. Zhou), xujg1982@connect.hku.hk (J. Xu).

[1] HaoRan Du, Bang Li, and Rui Yu contributed equally to this work.

https://doi.org/10.1016/j.bioactmat.2024.02.014
Received 25 November 2023; Received in revised form 23 January 2024; Accepted 11 February 2024

Abbreviations full forms

ALP	Alkaline phosphatase
ARS	Alizarin red staining
BMD	Bone mineral density
BS/TV	Bone surface/total volume
BV/TV	Bone volume/total volume
CCK-8	Cell Counting Kit-8
Dox	Doxycycline
DPSCs	Dental pulp stem cells
ECAR	Extracellular acidification rate
EDS	Energy-dispersive X-ray spectroscopy
ELISA	Enzyme-linked immunosorbent assay
ETV2	ETS variant 2
H&E	Hematoxylin-Eosin
HA/CS MS	Hydroxyapatite/chitosan microspheres
HIF-1α	Hypoxia-inducible factor-1α
HSCs	Hematopoietic stem cells
HUVEC	Human umbilical vein endothelial cells
OCR	Oxygen consumption rate
PHD2	Prolyl hydroxylas 2
PI	Propidium iodide
qRT-PCR	Quantitative Real-time Polymerase Chain Reaction
ROS	Reactive oxygen species
siRNA	Short interfering RNA
TAC	Tricarboxylic acid cycle
Tb Th	Trabecular thickness
TEM	Transmission electron microscopy
VEGFA	vascular endothelial growth factor A
WB	Western blot
XRD	X-ray diffraction analysis
α-KG	α-ketoglutarate

translational application [5–8].

Energy metabolism forms the foundation of diverse biological processes and is a prerequisite for physiological functions. Post bone injury, mesenchymal stem cells (MSCs) undergo osteogenic lineage commitment and differentiate into functional osteocytes to form new bone. However, compared to the adipogenic differentiation of MSCs, osteoblast-related cell proliferation and differentiation are energy-intensive processes that require consistently active metabolism to meet energy demands [9,10]. Bioenergy mapping studies have demonstrated that initiation of osteogenic differentiation of MSCs necessitates accelerated oxidative phosphorylation and glycolysis [11,12]. However, high-energy metabolism produces secondary high intra-mitochondrial reactive oxygen species (ROS), which damages the mitochondria and limits the energy supply [13]. When the energy supply is compromised, MSC proliferation and differentiation are hindered, resulting in delayed tissue repair and exacerbation of the original damage [12]. Therefore, a key target for promoting bone regeneration is to ensure an adequate energy supply to support MSC osteogenic differentiation.

Microcirculation disruption caused by bone fractures leads to a critical hypoxic microenvironment [14]. Under hypoxic conditions, reactive hypoxia-inducible factor-1α (HIF-1α) activation induces metabolic reprogramming in osteoblasts, shifting from aerobic respiration to anaerobic glycolysis [15]. This adaptation enhances cell survival and resistance to hypoxic microenvironments. Additionally, within the skeletal system, HIF-1α plays a crucial role in H-type capillary formation, which create distinct metabolic and molecular microenvironments that facilitate angiogenesis and osteogenesis coupling [16]. Some studies have explored bioinspired strategies involving materials equipped with HIF-1 pathway agonists, significantly contributing to local angiogenesis and bone regeneration [17,18]. However, burst release and excessive local concentrations of agonists can lead to histotoxicity. Therefore, gaining a comprehensive understanding of the cell types mediated by hypoxic signals within the microenvironment to precisely activate HIF-1 signaling is imperative [19]. MSCs play a pivotal role in regenerative medicine. Human dental pulp contains precursor cells known as dental pulp stem cells (DPSC), which exhibit self-renewal and multilineage differentiation abilities and share phenotypic and morphological characteristics with MSCs. Focusing on MSCs, our research has unveiled that ETS variant 2 (ETV2) regulates intracellular HIF-1α homeostasis and influences hypoxia signaling within the bone niche, thereby expediting vascularized bone regeneration.

ETV2 is a transcription factor that regulates the endothelial and hematopoietic development [20]. Herein, we have discovered that ETV2 serves as a pivotal transcription factor for energy metabolic reprogramming, linking osteogenic and angiogenic processes via hypoxic signaling. Osteogenic lineage differentiation of MSCs is accompanied by high ETV2 expression. DPSC exhibit self-renewal and multilineage differentiation abilities. They are more readily available and share phenotypic characteristics with MSCs. In adult DPSCs with limited inherent regenerative potential, ETV2 transient activation maintains intracellular HIF-1α homeostasis and promotes osteogenic differentiation through the prolyl hydroxylase 2 (PHD2)–HIF–1α-vascular endothelial growth factor A (VEGFA) axis. Furthermore, reduced α-ketoglutarate (α-KG) release from ETV2-mediated DPSCs creates a hypoxic signal-homeostatic angiogenic niche, thereby promoting endothelial cell migration and the rapid formation of vascular structures. ETV2 orchestrates metabolic reprogramming by simultaneously accelerating oxidative phosphorylation and glycolysis to enhance energy supply and rate of regeneration.

Microspheres are expected to reconstruct native stem cell niches, supporting the regulatory functions and metabolic activity of MSCs in the microenvironment [21,22]. We utilized hydroxyapatite/chitosan microspheres to deliver ETV2-DPSCs/MS complexes to critically sized rat cranial defect models, resulting in accelerated bone regeneration. Therefore, we present an effective application strategy that simultaneously achieves rapid angiogenesis and bone regeneration, driven by the regulation of local hypoxic signaling homeostasis and energy metabolism programming. This approach holds significant promise for treating bone defects, particularly critical-size bone defects.

2. Materials and methods

2.1. Cell culture

Human DPSC were obtained from Procell Life Science and Technology Co. (China). To identify stem cell surface markers, flow cytometry detected FITC-conjugated surface antibodies (CD90 (328,107, Biolegend), CD73 (344,015, Biolegend), CD44 (397,517, Biolegend), CD31 (303,103, Biolegend), CD45 (304,005, Biolegend), and CD34 (343,603, Biolegend)). For osteogenic differentiation induction, DPSCs were cultured in a complete medium with 10 mM β-glycerophosphate, 10^{-7} M dexamethasone, and 50 μg/ml ascorbic acid.

Human umbilical vein endothelial cells (HUVEC) were purchased from Thermo Scientific and cultured in an Endothelial Cell Medium (Gibco). The cell line was qualified post authentication and tested negative for mycoplasma.

2.2. Lentivirus transfection

An ETV2-encoding lentivirus based on doxycycline (Dox) induced (GeneChem, China) and EGLN1(PHD2)-encoding lentiviruses (Genomeditech, China) was constructed. During transfection, when cell

fusion reached 30–50%, cells were transfected with lentivirus using 5 μg/ml polybrene. After 12 h, the medium was replaced with complete medium. To ensure constant ETV2 expression in ETV2-DPSCs, 100 ng/ml Dox was incorporated. For VEGFA and PHD2 knockdown, cells were grown to 80% confluence and transfected with short interfering RNA (siRNA), including human-si-NC, human-si-VEGFA, and human-si-EGLN1 (provided by Tsingke Biotech, China), using 2.5 μg/ml lipofectamine 2000 (Invitrogen). The plasmid sequences are depicted in the Supplementary Material.

2.3. Quantitative real-time polymerase chain reaction (qRT-PCR)

Total RNA was extracted using TRIzol (Invitrogen) and the mRNA concentration was quantified using a NanoDrop2000 spectrometer. Subsequently, cDNA was synthesized using the PrimeScript-b® RT reagent Kit (TaKaRa Biotech, Japan). To evaluate the expression of the target genes, polymerase chain reaction (PCR) was conducted using the TB Green Premix ExTapTM II kit (TaKaRa Biotech) following the SYBR protocol. The cycling condition was as follows: 95 °C for 5 min, followed by 30 cycles of 98 °C for 10 s, 55 °C for 10 s, 72 °C for 90 s, and 1 cycle of 72 °C for 8 min. The results were evaluated by the $2^{-\triangle\triangle}$CT method, with GAPDH serving as the reference gene. Primer sequences for the evaluated genes are enlisted in Table 1.

2.4. Western blot

Total cellular protein was extracted using RIPA lysis buffer (Beyotime, Shanghai, China) supplemented with a protease inhibitor cocktail (Beyotime) (see Table 2). Cytoplasmic and nuclear proteins were separately extracted according to the manufacturer's instructions using the NE-PER™ Nuclear and Cytoplasmic Extraction Reagents (Thermo Scientific). Subsequently, the proteins (12 μg) were separated on 10–12% (w/v) SDS-polyacrylamide gel (Beyotime) and transferred onto a PVDF membrane. The membrane was blocked with 5% (w/v) fetal bovine serum (BSA) for 1 h at room temperature and then incubated overnight at 4 °C with primary antibodies specific for ETV2 (ab181847, 1:1000, Abcam), OSX (ab209484, 1:1000, Abcam), RUNX2 (ab76956, 1:1000, Abcam), OPN (NB110-89062, 1:1000, Novus), Collagen 1 (ab255809, 1:1000, Abcam), HIF-1α (BF8002, 1:1000, Affinity), PHD1 (EGLN2, DF7918, 1:1000, Affinity), PHD2 (DF6285, 1:1000, Affinity), PHD3 (DF12694, 1:1000, Affinity), VEGFA (66828-1-Ig, 1:1000, Proteintech), ERK1/2 (YT1625, 1:1000, ImmunoWay), pERK1/2 (YP1055, 1:1000, ImmunoWay), VE-Cadherin (AF6265, 1:1000, Affinity), AIF (sc-13116, 1:1000, Santa), Mitofilin (sc-390,707, 1:1000, Santa), and β-actin (ZSGB-Bio). The samples were then incubated with a secondary antibody (1:10,000, ZSGB-Bio) for 1 h and visualized using an ECL kit (Millipore).

2.5. Alkaline phosphatase (ALP) and alizarin red S staining (ARS)

Post osteogenic induction, the DPSCs were fixed with 4% paraformaldehyde and stained using an alkaline phosphatase activity kit (Beyotime) and Alizarin red S solution (ServiceBio), following the manufacturer's instructions. To quantify mineral deposition, the mineralized matrix was destained using 10% cetylpyridinium chloride (Sigma-Aldrich) and the absorbance of the solution was quantified at 562 nm using an enzyme-labeled instrument.

Table 1
Primer sequences.

Gene	Forward sequence	Reverse sequence
ETV2	GAAGGAGCCAAATTAGGCTTCT	GAGCTTGTACCTTTCCAGCAT
RUNX2	TGGTTACTGTCATGGCGGGTA	TCTCAGATCGTTGAACCTTGCTA
OSX	CCTCTGCGGGACTCAACAAC	AGCCCATTAGTGCTTGTAAAGG
COL1A1	GAGGGCCAAGACGAAGACATC	CAGATCACGTCATCGCACAAC
OPN	CTCCATTGACTCGAACGACTC	CAGGTCTGCGAAACTTCTTAGAT
PHD1	TGGCCCTGGACTATATCGTG	GGCACCAATGCTTCGACAG
PHD2	GAAGGCGAACCTGTACCCC	TTCATGCACGGCACGATGTA
PHD3	CTGGGCAAATACTACGTCAAGG	GACCATCACCGTTGGGGTT
HIF-1α	GAACGTCGAAAAGAAAAGTCTCG	CCTTATCAAGATGCGAACTCACA

Table 2
Plasmid sequences.

gene	Sense (5′-3′)	Antisense (5′-3′)
Human-si-VEGFA	CAAGAUCCGCAGACGUGUA (dT) (dT)	UACACGUCUGCGGAUCUUG (dT) (dT)
Human-si-PHD2	CAAGGUAAGUGGAGGUAUA (dT) (dT)	UAUACCUCCACUUACCUUG (dT) (dT)

2.6. Mouse tooth extraction model

All in vivo procedures involving laboratory animals were approved by the Ethics Committee of the Capital Medical University (KQYY-202304-005). The animals were obtained from the Animal Experimental Center of Capital Medical University and were uniformly cared for by the animal experimental center. The animal studies complied with the Animal Research: Reporting In Vivo Experiments (ARRIVE) 2.0 guidelines.

Twenty male mice, aged 7–8 weeks, were used for tooth extraction. Mice were anesthetized via intraperitoneal sodium pentobarbital (100 mg/kg) injection. After administering anesthesia, the oral cavity underwent disinfection, and the maxillary first molars on both sides were extracted using apical elevator, ensuring an examination of tooth root integrity. Local compression was applied as needed to control bleeding, ensuring the formation of blood clots within the extraction sockets and preventing active bleeding. Postoperatively, mice were offered a soft diet to facilitate recovery.

2.7. Tissue preparation and histological observation

The tissue samples were processed as follows: they were initially fixed in 4% paraformaldehyde for 24 h, then embedded in paraffin, and subsequently sectioned into 5-μm thick slices. For hard tissues, extensive decalcification was conducted using 14% EDTA solution (pH 7.4) for four weeks before embedding.

Hematoxylin-Eosin (H&E) and Masson staining were conducted on all serial sections. For immunofluorescence, sections or cells were incubated with primary antibodies, including ETV2 (ab181847, 1:500, Abcam), CD90 (105,201, 1:100, Biolegend), pERK1/2 (YP1055, 1:100, ImmunoWay), HIF-1α (BF8002, AF1009, 1:100, Affinity), PHD2 (DF6285, 1:100, Affinity), CD31 (AF6191, 1:100, Affinity), OPN (NB110-89062, 1:100, Novus), and Collagen I (AF7001, 1:100, Abcam) overnight at 4 °C. Subsequently, secondary antibodies, including FITC-Conjugated Goat anti-mouse IgG (HA1003, 1:200, HUABIO), Alexa Fluor 594 Anti-rabbit IgG (8889, 1:500, Cell Signaling Technology), Alexa Fluor 488 Anti-rabbit IgG (4412, 1:500, Cell Signaling Technology), and FITC-conjugated goat anti-rabbit IgG (SA00003-11, 1:100, Proteintech), were applied for 1 h. Nuclei were labeled with DAPI (Beyotime) for 5 min and images were captured using a fluorescence microscope (Leica).

2.8. RNA extraction, library construction, and sequencing

Total RNA was extracted using the TRIzol reagent kit (Invitrogen) post 7 d of osteogenic differentiation induction. RNA quality was assessed with an Agilent 2100 Bioanalyzer (Agilent Technologies, USA) and checked using RNase-free agarose gel electrophoresis. Post total RNA extraction, eukaryotic mRNA was enriched using oligo (dT) beads. The enriched mRNA was converted into short fragments using fragmentation buffer and reverse-transcribed into cDNA using the NEBNext Ultra RNA Library Prep Kit for Illumina (NEB#7530, USA). The purified

double-stranded cDNA fragments underwent end-repair, had an A base incorporated, and were ligated to Illumina sequencing adapters. The ligation reaction mixture was purified using AMPure XP Beads (1.0*X*). The ligated fragments were size selected by agarose gel electrophoresis and PCR amplification. The resulting cDNA library was sequenced using an Illumina Novaseq6000 (Gene Denovo Biotechnology Co.).

2.9. Dual-luciferase reporter assay

The putative binding regions of ETV2 in the human PHD2 promoter were amplified from genomic DNA and mutant fragments of the high-score-binding regions were generated using PCR. Target fragments were then inserted downstream of the firefly luciferase (FL) gene into the pGL3-basic luciferase reporter vector (Genomeditech) using seamless cloning. For luciferase reporter assays, 293 T cells were co-transfected with individual plasmids, including pGL3-PHD2, pGL3-PHD2-MT1, pGL3-PHD2-MT2, and ETV2, using Lipofectamine 2000. After 48 h post-transfection, cell lysates were collected and assayed using a Dual-Luciferase Assay kit, according to the manufacturer's instructions. The results were normalized using Renilla luciferase (RL) relative light units and presented as the ratio of FL/RL activity.

2.10. Bioenergetic analyses

To evaluate the impact of ETV2 on DPSC energy metabolism, we conducted oxygen consumption (OCR) and extracellular acidification rate (ECAR) assays using the Mito-stress and Glycolysis Stress Test Kits, respectively, which were conducted using the Seahorse Bioscience XFe96 Extracellular Flux Analyzer (Agilent). DPSCs were subjected to osteogenic differentiation for diverse durations, including 12 h, 1, 3, 7, and 14 d. Subsequently, the cells were seeded in 96-well plates (Agilent Technologies) at 5000 cells/well density. After washing thrice, the OCR was measured by sequentially incorporating 2 μM oligomycin, 2 μM FCCP, and 1 μM Rotenone & antimycin A, per a previously described protocol [10]. Afterward, 10 mM glucose, 2 μM oligomycin, and 50 mM 2-DG were introduced to evaluate ECAR. The OCR and ECAR values were computed post normalization using the Cell Counting Kit-8 (CCK-8) assay results.

Mitochondrial morphology was assessed through transmission electron microscopy (TEM) scanning, following the sample preparation guidelines and procedures provided by Servicebio. To evaluate the functional status of the mitochondria, we employed Rhodamine 123 staining (Beyotime), a superoxide Assay Kit (Beyotime), and a ROS Assay Kit (Beyotime), adhering to the manufacturer's instructions. The absorbance and fluorescence values were normalized to the CCK-8 assay results.

2.11. Enzyme-linked immunosorbent assay (ELISA)

For ELISA experiments, cell supernatant samples from an equal number of cells were processed by centrifugation to remove particulate matter and then triple-diluted. Additionally, cell lysate samples were obtained by subjecting 1×10^4 digested cells to repeated freeze-thaw cycles. We used a Human VEGF-A Pre-coated ELISA Kit (1,117,342, Dakewe) to detect both intracellular and secretory VEGFA. The standard was gradient diluted to create a standard curve. After reacting with the reaction well and enzyme-labeled antibody, the sample was subjected to coloration using the substrate. The reaction was terminated by incorporating a stopping solution. The absorbance was measured at 450 nm using an enzyme-labeled instrument and the actual concentration was computed based on a standard curve.

α-Ketoglutarate (α-KG) content in the supernatant was determined using the Alpha Ketoglutarate Assay kit (ab83431, Abcam) through colorimetry. According to the operating manual, the α-KG standard was gradient-diluted to create a standard curve. The supernatant samples were centrifuged to remove impurities, deproteinized, adjusted PH to 6.5–8, and incubated with a colorimetric reaction system for 30 min in the dark. Post incubation, the absorbance of the samples was measured at 570 nm using an enzyme-labeled instrument. The actual α-KG concentration in the samples was determined using a standard curve.

2.12. Angiogenesis assay

A tube formation assay was conducted to assess angiogenesis. Initially, 1×10^4 human umbilical vein endothelial cells (HUVECs) were seeded onto a 96-well plate, which was pre-coated with a 50 μl layer of Matrigel matrix (Corning). Diverse cell supernatants, 100 μM/ml α-KG (MCE), and 10 nM/ml IOX4 (a competitive inhibitor of α-KG, MCE) were incorporated to diverse experimental groups. The HUVECs were then incubated at 37 °C for 16 h and tube formation was subsequently observed. To quantitatively assess angiogenesis, the number of nodes formed in the tubes was evaluated. This analysis was conducted using ImageJ software and involved selecting four randomly chosen fields for each sample to determine the number of nodes within these areas.

2.13. Wound healing assay

When the HUVECs reached 90% confluence, a pipette tip was used to create a controlled scratch in the central region of the cell monolayer. Subsequently, cell quintuple-dilution supernatant from diverse treatment groups, including, 100 μM/ml α-KG and 10 nM/ml IOX4, was incorporated to the respective experimental groups. After a 16-h incubation period, the relative area covered by migrating cells was carefully observed. To quantify the extent of cell migration, the relative area of cell migration was assessed using ImageJ software.

2.14. Cell proliferation assays

HUVECs were seeded into 96-well plates at 5000 cells/well density, and each group was subjected to diverse treatments as indicated. At specified time points, 10 μL CCK-8 reagent (MCE) was mixed with 90 μL medium and incorporated to the cells. This mixture was then incubated with the cells at 37 °C for 2 h. Following incubation, absorbance was determined at 450 nm using an enzyme-labeled instrument.

2.15. Matrigel plug assay in vivo

In vivo angiogenesis was assessed using the Matrigel plug assay. Twenty female BALB/c nude mice were randomly allocated to four experimental groups. Each group received an injection of a complex comprising 3×10^6 HUVECs, 300 μL Matrigel, along with either cell supernatant or specific stimulants into the subcutaneous regions in the underarms of mice. After seven days, the implanted tissues were surgically retrieved, the extent of angiogenesis was examined based on tissue dimensions, and immunofluorescence was used to label the vascular markers. Neovascularization within the Matrigel plugs was quantified using the ImageJ software.

2.16. Preparation of hydroxyapatite chitosan microspheres (HA/CS MS)

In 1 L of 1% (v/v) acetic acid solution, 1 g chitosan powder and 1 g nano-hydroxyapatite were successively dissolved and sonicated for 10 min to obtain an aqueous 1 % (w/v) HA/CS solution. The oil phase was prepared by incorporating 3% (v/v) Span-80 to cyclohexane. The flow rates of the outer oil and inner water phases were set to 1.0 and 0.05 ml/min. The typical pore sizes were 300–400 and 60–90 μm. NaOH powder (6 g) was dissolved in ethanol (500 ml) to form a 0.3 M NaOH-ethanol solution to collect the dripping HA/CS emulsion, which was subsequently washed with ethanol. The pellets were collected by centrifugation at 5000 rpm for 15 min, washed thrice with distilled water, and freeze-dried to obtain HA/CS-MS.

2.17. Characterization and in vitro HA/CS MS biocompatibility

Scanning electron microscopy (SEM) samples were fixed in a 2.5% (v/v) glutaraldehyde solution for 24 h. Post fixation, the samples were thoroughly rinsed with deionized water to remove excess fixative. After washing thrice with 100% sodium *tert*-butoxide, the samples were freeze-dried. Post freeze-drying, the samples were prepared by ion sputtering. They were imaged with the SEM, a Gemini 500 SEM (Zeiss, Germany).

Following freeze-drying, the microspheres underwent compositional analysis using X-ray diffraction analysis (XRD). The ratio of inorganic to organic components in the composite microspheres was investigated using thermogravimetric analysis. Energy-dispersive X-ray spectroscopy (EDS) analysis was employed to observe the distribution of nitrogen (N), calcium (Ca), phosphorus (P), and sodium (Na) elements on the microsphere surface. An atomic force microscope was used to test the mechanical strength of microspheres. The Young's modulus of microspheres was determined using NanoScopeAnalysis software.

CCK-8 assay: To evaluate cell viability, DPSCs were co-cultured with microspheres in 96-well plates at 5000 cells per well density. The detailed detection method for cell viability was identical to that used for the cell proliferation assays.

Live-dead staining: The staining solution was prepared by mixing 2 μL calcein acetoxymethyl and 3 μL propidium iodide (PI) in 1 ml PBS. The cell samples were stained for 15 min at room temperature and observed under a fluorescence microscope. During staining, dead cells fluoresced red, whereas living cells fluoresced green.

Immunofluorescence: To assess the effects of the microsphere surface environment on osteogenic differentiation, DPSCs were cultured with 2 $\times$ 10^5 cells and 100 μL microspheres in a six-well plate without adhesive coating for one day. Osteogenic induction was conducted for 7 d, and immunofluorescence was performed to detect RUNX2 and OSX.

2.18. Rat critical-size calvarial defect model

Cells (1 $\times$ 10^6) were incubated with 1 ml scaffold for 1 d to form DPSC/MS complexes, which were later used to evaluate vascularized bone regeneration in vivo. Before in vivo transplantation, the complexes were subjected to 7 d of osteogenic induction.

In the calvarial defect model, 8-week-old male Sprague-Dawley rats, weighing 200–220 g, were randomly assigned to four groups, each comprising six rats: Control, MS, NC-DPSCs/MS, and ETV2-DPSCs/MS. Surgical procedures were conducted under anesthesia with 3% (w/v) pentobarbital sodium following established protocols [23]. A sagittal incision was made in the middle of the calvaria, and a 5-mm diameter bicortical, extradural defect was created on one side of the parietal bone using a dental trephine drill, with precooled saline applied to prevent overheating of the bone margins. All defects, except those in the control group, were covered with the corresponding materials. Finally, the periosteum was reset, and careful tension-free suturing of both the periosteum and skin was performed. The entire procedure was conducted gently to avoid any displacement of materials. Uniform care procedures and measures were implemented across all groups.

2.19. Bone regeneration analysis

Micro-CT scanning: It was conducted 4 weeks post-surgery using the SkyScan 1176 Micro-CT scanning system (Bruker, Germany) to reconstruct a 3D image of the regenerated tissue. The scanning parameters comprised a 90 kV X-ray source and 9 μm resolution. Bone microparameters within the target area were evaluated using systematic analysis software to assess key parameters, including bone mineral density (BMD), bone volume/total volume (BV/TV), bone surface/total volume (BS/TV), and trabecular thickness (Tb Th).

Histology: Post scanning, the specimens were decalcified and sectioned for histological observation by H&E and Masson staining. To ascertain the impact of osteogenesis and angiogenesis, the presence of RUNX2, OSX, CD31, OPN, and Collagen I was established using immunofluorescence, employing the previously mentioned method. To precisely quantify the extent of positive staining, ImageJ software was used to scrutinize five randomly selected visual fields.

2.20. Statistical analysis

All quantitative measurements were presented as mean ± standard deviation. All statistical analyses were conducted using Prism 6.0 software. Student's t-test and analysis of variance (ANOVA) were used for paired and multiple comparisons, respectively. The threshold for statistical significance was set at $P < 0.05$.

3. Results

3.1. ETV2 exhibits high expression during the early stages of intramembranous ossification, and it enhances DPSC osteogenic differentiation

MSCs play a pivotal role in facilitating bone regeneration by undergoing phenotypic transformation into osteoblasts and subsequent differentiation into mature osteoblasts, thereby promoting bone formation. This phenomenon is consistent with the intramembranous ossification observed in vivo. The tooth extraction model is considered a representative model of intramembranous ossification, offering a robust means of effectively simulating and assessing the intramembranous ossification processes [24]. To investigate the potential alterations in ETV2 expression during intramembranous ossification and their impact on this process, we examined the expression pattern of ETV2 in MSCs during the regenerative phase using a tooth extraction model.

Histological observations were conducted post bilateral extraction of the maxillary first molars at 1, 3, 7, and 14 d post-surgery. H&E staining revealed that on day 1, the extraction socket was filled with blood clots and few cellular components were present. By day 3, substantial infiltration of immune cells was observed. By day 7, finger-like woven bones had begun to form, and by day 14, mature lamellar bones had formed with ongoing bone remodeling (Fig. 1A). This sequence of events signifies the phases of healing including an inflammatory phase, a proliferative phase, and bone modeling and remodeling, with the 7-d period marking primary osteon formation and representing the early stage of overall bone regeneration [25]. On postoperative days one and three, a limited number of $CD90^+$ MSCs migrated from the root tip to the extraction socket. By day 7, a significant increase was observed in $CD90^+ETV2^+$ MSCs distributed within the osteoblastic niche along the edges of the finger-like bone. This indicated that the MSCs were committed to osteogenic differentiation. As the process transitioned to the bone remodeling stage on day 14, $CD90^+ETV2^+$ MSC population declined rapidly (Fig. 1A).

To further explore ETV2 expression during DPSC osteogenic differentiation, we isolated and characterized human DPSCs. These DPSCs exhibited robust expression of MSC-related markers, including CD90, CD73, and CD44, while CD31, CD45, and CD34 expressions were low (Fig. S1A). Furthermore, we validated the differentiation potential of the DPSCs using a tri-lineage differentiation assay (Fig. S1B). Following osteogenic induction of DPSCs for 21 d, we observed that endogenous ETV2 levels increased to 3.05 ± 0.28-fold at day 7, subsequently returning to control levels at days 14 and 21 (Fig. 1B). These findings indicate that ETV2 accumulates during the early stages of in vivo osteogenesis and osteogenic differentiation of DPSCs *in vitro*.

Osteoblast differentiation is a prerequisite for efficient bone regeneration. We first investigated the role of ETV2 in DPSC osteogenic differentiation. We employed a controllable overexpression system for ETV2, enabling stable ETV2 overexpression under the induction of 100 ng/ml Dox at both the mRNA and protein levels (Fig. S1 C, D). ALP staining after 7 and 14 d of osteogenic induction demonstrated that

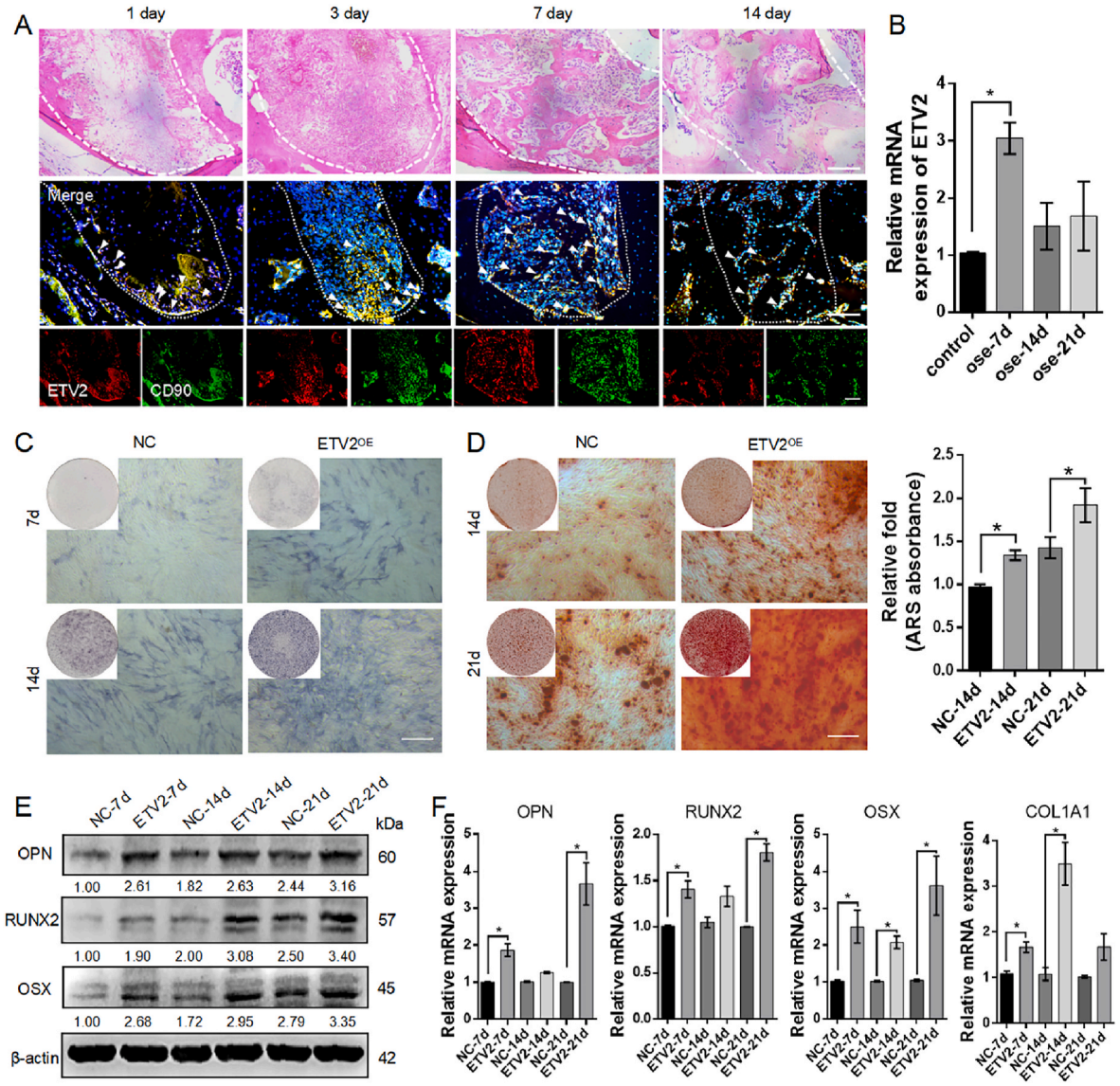

Fig. 1. Expression pattern of ETV2 and its enhancing effect on osteogenic differentiation of DPSCs (A) Representative images of H&E staining and immunofluorescence co-staining for ETV2 (red) and CD90 (green) at diverse time points (1, 3, 7, and 14 d) post-surgery in a mouse tooth extraction model. The white arrows represent positively stained cells. Scale bar: 100 μm (B) The mRNA expression pattern of ETV2 during DPSC osteogenic differentiation (C) Representative image of ALP staining (D) Representative image and semi-quantitative analysis of ARS staining. Scale bar: 200 μm (E) The protein expression of key osteogenic markers, RUNX2, OSX, and OPN post ETV2 overexpression (F) The mRNA expression of RUNX2, COL1A1, OSX, and OPN, post ETV2 overexpression (NC, negative control; OE, overexpression. Data are presented as the mean of >3 independent experiments ±SD. *P < 0.05, **P < 0.01).

ETV2-DPSCs exhibited significantly higher ALP activity (Fig. 1C). This heightened ALP expression indicates that ETV2-DPSCs are committed to the osteoprogenitor lineage at a faster rate, becoming preosteoblasts, than NC-DPSCs [26]. ARS staining at 14 and 21 d post osteogenic induction revealed that ETV2 enhanced mineralized matrix formation in mature osteoblasts (Fig. 1D). Furthermore, the expression of markers associated with osteoblast precursors (RUNX2 and OSX) and osteocytes (COL1A1 and OPN) was assessed at 7, 14, and 21 d [26]. Western blotting and qRT-PCR demonstrated that ETV2 significantly enhanced their expression at mRNA and protein levels (Fig. 1E, F and Fig. S8A). Collectively, these data indicate that ETV2 is essential for osteogenic differentiation and mineralization of DPSCs.

3.2. *ETV2 facilitates stabilization and nuclear accumulation of HIF-1α by transcriptionally inhibiting PHD2 and phosphorylating ERK1/2*

To further investigate the potential mechanisms by which ETV2 promotes DPSC osteogenic differentiation, we conducted RNA sequence analysis of total RNA samples obtained from ETV2-DPSCs and NC-DPSCs post 7 d of osteogenic induction. The results indicated the dysregulation of 616 genes, with 335 upregulated and 281 downregulated. KEGG functional enrichment analysis highlighted significant enrichment in pathways related to cytokine interactions and metabolism, with a particular emphasis on the HIF-1 signaling pathway (Fig. 2A). We assume that HIF-1 signaling pathway activation in MSCs may contribute to the coupling of bone regeneration and angiogenesis.

The family of PHDs degrades HIF-1α under normoxic conditions through oxygen-dependent hydroxylation of prolyl residues on HIF-1α. Within the PHD family, PHD2 is the most abundant member, and primarily contributes to this degradation [27]. A heatmap was generated to display genes associated with osteogenesis and HIF-1 signaling (Fig. 2B), revealing a significant EGLN1 (PHD2) downregulation, suggesting an impact on HIF-1α stabilization. Western blot analysis demonstrated that ETV2 overexpression led to a substantial increase in HIF-1α levels and a

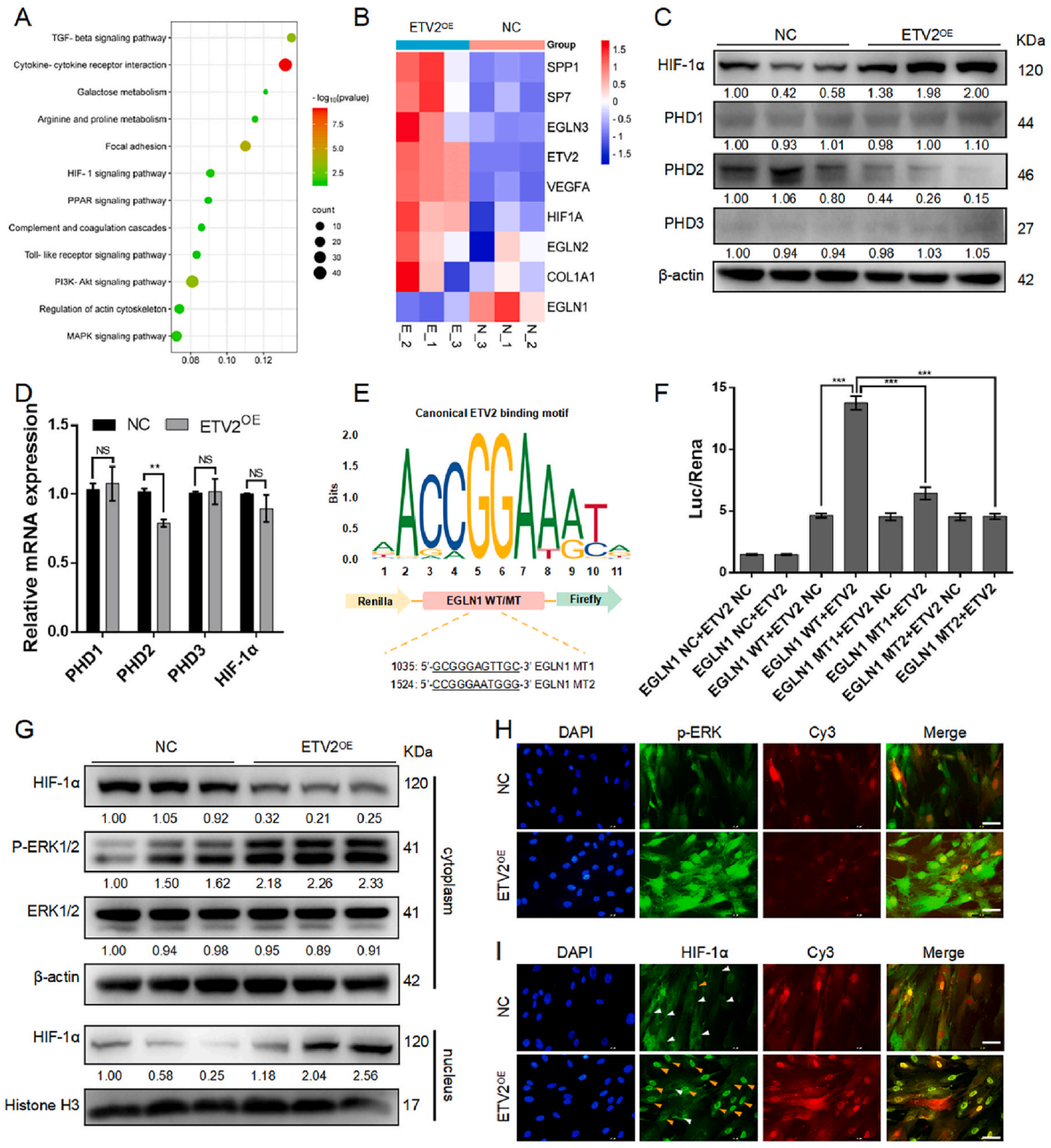

Fig. 2. ETV2 induces HIF-1α stabilization and nuclear accumulation by transcriptional inhibition of PHD2 and ERK1/2 phosphorylation (A) KEGG functional enrichment analysis of RNA sequence (B) A heatmap displays genes associated with osteogenesis and HIF-1 signaling (C, D) The protein and mRNA expression of HIF-1α and PHDs following ETV2 overexpression (E) Schematic of putative ETV2 binding elements on PHD2 promoter region (F) Dual luciferase reporter gene assay of ETV2 and PHD2 (G) Cytoplasmic HIF-1α, total and phosphorylated ERK1/2, and intracellular HIF-1α expression post ETV2 overexpression (H) Representative immunofluorescent images of intracellular phosphorylated ERK1/2. The Cy3 channel fluorescence represents lentiviral transfection. Scale bar: 50 μm (I) Representative immunofluorescent images of intranuclear HIF-1α. The Cy3 channel fluorescence represents lentiviral transfection. The orange arrows indicate the fluorescence of HIF-1α in the nucleus, while the white arrows point to the absence of HIF-1α fluorescence in the nucleus. Scale bar: 50 μm (NS, no significant difference, NC, negative control; OE, overexpression. Data are presented as the mean of >3 independent experiments ±SD. *P < 0.05, **P < 0.01, and ***P < 0.001).

decrease in PHD2 levels, and no significant differences were observed for PHD1 and PHD3 (Fig. 2C and Fig. S8B). At the mRNA level, ETV2 significantly affected PHD2 expression (Fig. 2D). Osteogenic induction was conducted under normoxic conditions, and this HIF-1α upregulation likely occurs indirectly due to PHD2 inhibition by ETV2. The regulatory mechanism by which ETV2 affects PHD2 is likely through transcriptional regulation, as analysis of the PHD2 promoter sequence revealed conserved putative ETV2 binding elements (Fig. 2E). Dual-luciferase reporter gene assays demonstrated that ETV2 increased luciferase activity driven by the PHD2 promoter. When the ETV2 binding elements were mutated to create a mutant PHD2 promoter construct, co-transfection with the ETV2 vector suppressed the luciferase activity of the mutant PHD2 promoter construct (Fig. 2F). In summary, ETV2 stabilizes HIF-1α levels through PHD2 transcriptional inhibition.

Our previous research has established that ETV2 promotes ERK1/2 phosphorylation, which may facilitate the formation of the HIF-1α and HIF-1β heterodimer and translocate into the nucleus for transcriptional activity [15,28]. Through the separation of cytoplasmic and nucleoprotein, we observed that ETV2 substantially increased intracellular phosphorylated ERK1/2 (pERK1/2) and intranuclear HIF-1α (Fig. 2G

and Fig. S8C) levels. Immunofluorescence analysis revealed strong fluorescence associated with pERK1/2 and intranuclear HIF-1α in the ETV2 OE group. Conversely, the NC group displayed a lack of intranuclear HIF-1α fluorescence (Fig. 2H and I). These data suggest that ETV2 induced nuclear translocation of HIF-1α by ERK1/2 phosphorylation.

3.3. The PHD2-HIF-1α-VEGFA axis plays a pivotal role in promoting DPSCs osteogenic differentiation

To assess changes in the HIF-1 signaling pathway during physiological osteogenesis, we examined PHD2 and HIF-1α expression in MSCs during the healing process following tooth extraction. The results revealed a significant increase in $CD90^{+}HIF\text{-}1\alpha^{+}$ cells in the early stages of osteogenesis (specifically, on post-extraction day 7) (Fig. 3A). The number of $CD90^{+}PHD2^{+}$ cells also increased (Fig. 3B). This contradictory outcome may be attributed to the incomplete formation of the vascular network, resulting in a relative lack of oxygen as a co-acting substrate, which leads to PHD2 dysfunction.

To further explore the impact of the PHD2-HIF-1α axis on DPSC osteogenic differentiation, we conducted gain-of-function and loss-of-function experiments. PHD2 overexpression resulted in significant reductions in mineralized nodules (Fig. 3C), including decreased levels of HIF-1α, VEGFA, and the osteoblast markers OPN and COL-1 (Fig. 3D and Fig. S8D). Conversely, PHD2 knockdown using siRNA led to enhanced osteogenic differentiation (Fig. S2).

HIF-1α stabilization leads to endogenous and secretory VEGFA upregulation (Fig S3A, B). Notably, the conditional knockout of VEGF in

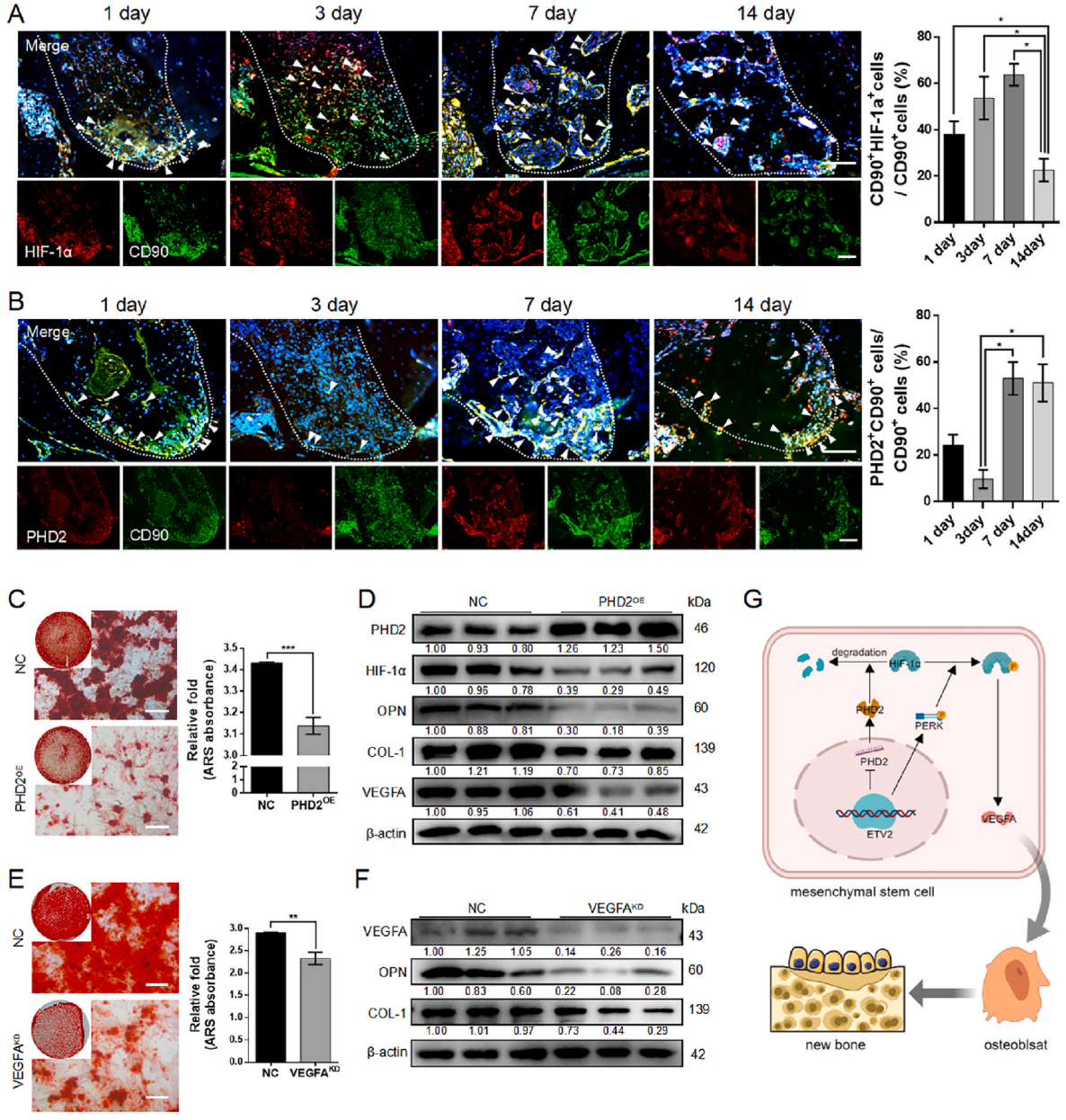

Fig. 3. PHD2-HIF-1α-VEGFA axis promotes DPSC osteogenic differentiation (A, B) Representative images and quantitative statistics of immunofluorescence co-staining HIF-1α (red) and CD90 (green), PHD2 (red), and CD90 (green) in a mouse tooth extraction model. The white arrows represent positively stained cells. Scale bar: 100 μm (C, E) Representative image and semi-quantitative analysis of ARS staining post PHD2 overexpression and VEGFA knockdown. Scale bar: 100 μm (D, F) The protein expression of HIF-1 signaling (PHD2, HIF-1α, and VEGFA) and osteogenic makers (COL-1 and OPN) post PHD2 overexpression and VEGFA knockdown (G) Schematic illustration of mechanism of osteogenesis by PHD2-HIF-1α-VEGFA axis (KD, knockdown; NC, negative control; and OE, overexpression. Data are presented as the mean of >3 independent experiments ±SD. *P < 0.05, **P < 0.01, and ***P < 0.001).

osteoblast cell lines results in mineralization defects that cannot be rescued, even with exogenous VEGFA supplementation [29]. The hTFtarget database indicates that VEGFA is the target coding protein of HIF-1α, and the physical binding of HIF-1α to VEGFA promoters has been verified through chromatin immunoprecipitation assays [30]. When endogenous VEGFA in DPSCs was knocked down using siRNA, the expression of mineralized matrix, OPN, and COL-1 significantly decreased (Fig. 3E, F and Fig. S8E). Moreover, upon the addition of an extra 40 ng/ml of VEGFA, there were no noticeable alterations in mineralized matrix and osteogenic protein expression compared to the control group (Fig. S3C-E). These findings imply that HIF-1α facilitates DPSCs osteogenic differentiation by elevating the intracellular levels of VEGFA. In summary, these findings partially elucidate the osteogenic effects of ETV2 on DPSCs through the PHD2-HIF-1α-VEGFA axis (Fig. 3G).

3.4. *ETV2 drives metabolism reprogramming and mitigates mitochondrial dysfunction, resulting in a reduction in α-KG release*

Respiration is essential for cell survival and function. Metabolic reprogramming induced by HIF-1 signaling promotes anaerobic glycolysis, a mechanism that supports osteoblast function [15]. Furthermore, RNA-seq analysis revealed a potential role of ETV2 at the metabolic level (Fig. 2A). This prompted us to investigate whether ETV2

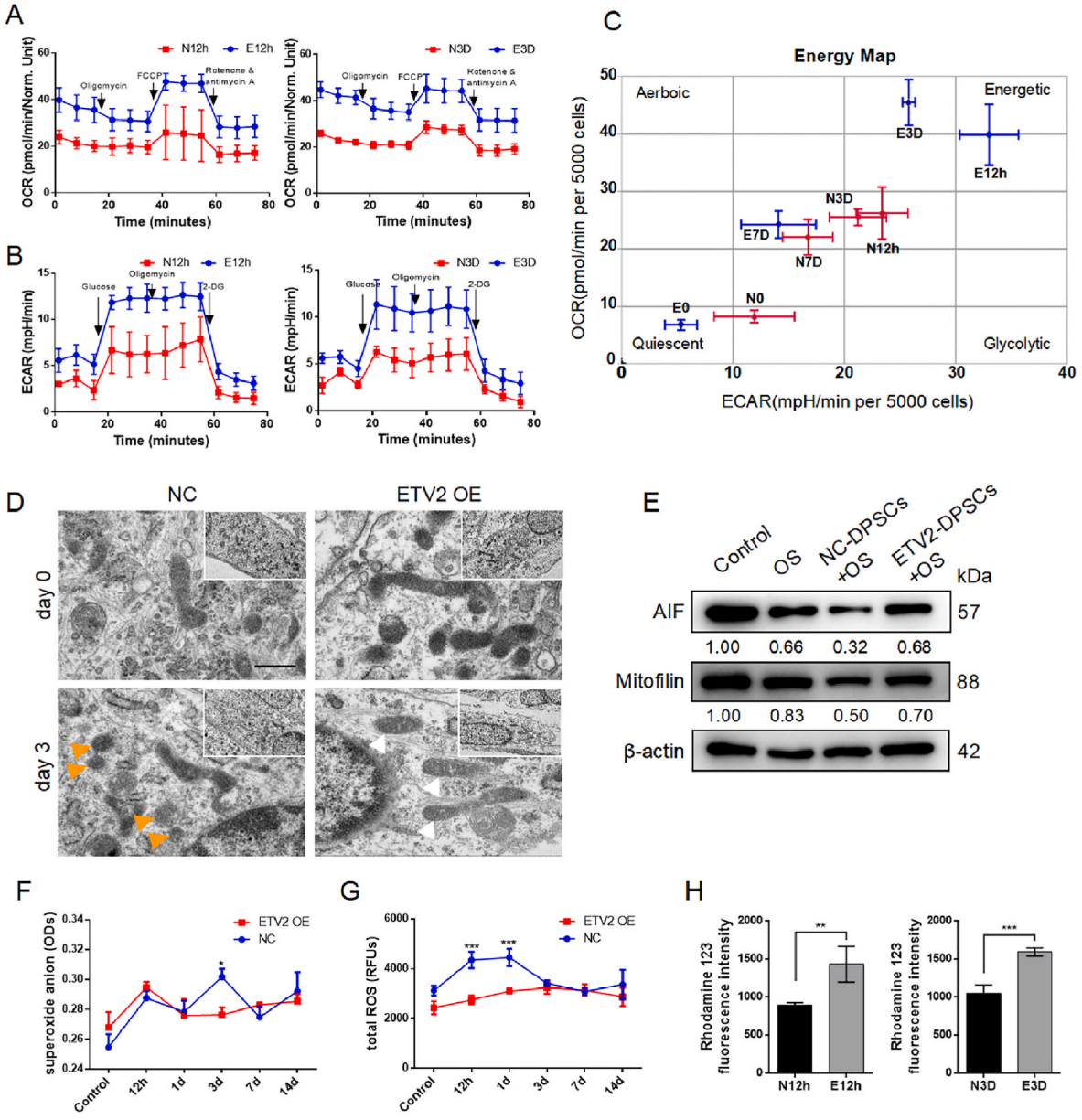

Fig. 4. ETV2 enhances energy metabolism and reduces mitochondrial dysfunction (A) OCR detection measures mitochondrial respiration in ETV2-DPSCs at diverse time points post osteogenic induction (B) The ECAR detection measures glycolysis stress in ETV2-DPSCs at diverse time points post osteogenic induction (C) Energy map based on the ATP rate (OCR/ECAR) of the energy metabolic pathway of NC-DPSCs and ETV2-DPSCs under osteogenic induction at diverse times (D) The transmission electron microscope (TEM) image reveals mitochondria ultrastructure in ETV2-DPSCs post 3 d of osteogenic induction. Mitochondria membrane damage is indicated by the orange arrows, while rod-like mitochondria are indicated by the white arrow. Scale bar: 500 nm (E) The protein expression of AIF and Mitofilin post osteogenic induction (OS) and ETV2 overexpression (F, G) An assessment of superoxide anion and total reactive oxygen species (ROSs) during DPSCs osteogenic differentiation (H) Mitochondrial membrane potential analysis indicated by fluorescence intensity of Rhodamine 123 post osteogenic induction for 12 h and 3 d (OS, osteogenic induction; NC, negative control; OE, overexpression. Data are presented as the mean of >3 independent experiments ±SD. *P < 0.05, **P < 0.01, and ***P < 0.001).

influenced tissue regeneration from metabolic regulation perspective. High-throughput Seahorse XF instruments are recognized as the gold standard for rapid analysis of theoretical glycolytic and oxidative fluxes [31]. To further validate the effects of ETV2 on the energy metabolism of DPSCs, OCR, and ECAR analyses were conducted at diverse time points during osteogenic induction. The results indicated that ETV2 promoted mitochondrial oxidative phosphorylation (OXPHOS) at the early stages of osteogenic induction (at 12 h and 3 d), which was reflected in increased basal and maximal mitochondrial respiration and ATP-linked respiration (Fig. 4A–C). In ECAR detection, ETV2 promotes glycolysis, glycolytic capacity, and glycolytic reserves at 12 h and 3 d (Fig. 4B). However, no significant differences were observed at the subsequent time points (Fig. S4). Given the antagonistic effect of HIF-1α on mitochondrial oxidative phosphorylation [9,32], it is noteworthy that the increase in mitochondrial aerobic respiratory appears to be independent of the HIF-1 signal, which may be associated with mitochondrial function protection.

Subsequently, we conducted an in-depth examination of mitochondrial ultrastructure and function. Three days post osteogenic induction, TEM morphological analysis revealed that mitochondria in the NC group demonstrated significant swelling and membrane damage, whereas mitochondria in the ETV2 group demonstrated no significant swelling (Fig. 4D). The Western blot results indicate that osteogenic induction leads to a significant decrease in mitochondrial membrane stability-related proteins, AIF, and Mitofilin. However, ETV2 can partially rescue the expression of AIF and Mitofilin, suggesting that ETV2 promotes mitochondrial membrane stability, preventing structural damage (Fig. 4E and Fig. S8F). Analyses of superoxide anions, total ROS, and mitochondrial membrane potential indicated that ETV2 had a protective effect against mitochondrial oxidative damage and apoptosis in the early stages of osteogenesis (Fig. 4F–H). These findings suggest that ETV2 may enhance the energy supply to meet the energy requirements for osteogenic lineage differentiation and improve the survival of MSCs by activating the HIF-1 pathway and preventing mitochondrial dysfunction.

Functional interactions between HIF-1α and tricarboxylic acid cycle (TAC) intermediates have been documented. For, example, the accumulation of succinate, fumarate, and L-2-hydroxyglutarate inhibits PHD activity, thereby enhancing the stability of HIF-1α within the subunit [33]. In this context, α-KG, which serves as both a co-acting substrate for PHD2 and an intermediate in TAC, is particularly relevant. Notably, reduced α-KG accumulation resulted from a faster TAC cycling process, and α-KG release into the surrounding microenvironment is assumed to be linked to mitochondrial damage [34,35]. The decrease in α-KG levels within the niche, resulting from the effects of ETV2 on mitochondria protection and enhanced OXPHOS, might contribute to the maintenance of local hypoxia signal homeostasis, manifesting in HIF-1α stabilization by PHD2 dysfunction. Our analysis revealed that α-KG concentration in NC-DPSC supernatant was higher, 2.96 ± 0.33 times that of the ETV2 OE group (Fig. 5B).

3.5. Reduction of α-KG induces angiogenesis

Osteoblastic cells have an impact on hematopoietic stem cell frequency in vivo [36]. Immunofluorescence co-staining with CD90 and CD31 revealed the proximity of MSCs to endothelial cells (Fig. 5A), which formed the foundation for physiological interactions within these niches. Although direct contact between hematopoietic stem cells (HSCs) and osteoblasts has seldom been observed using in vivo imaging in previous studies [37,38], the spatial relationship between MSCs and blood vessels suggests that MSCs may establish specialized niches to facilitate peripheral endothelial cells migration.

To investigate the pro-angiogenic role of ETV2-DPSCs within niches and the influence of α-KG on this process, we employed a tube formation assay. The number of tube nodes reflected the initiation of tube formation. HUVECs treated with ETV2-DPSC supernatant formed extensive tube structures and increased the number of nodes. This effect was attenuated by the incorporation of α-KG and partially rescued by IOX4, a competitive inhibition of α-KG (Fig. 5C–G). The wound healing assay mimicked the recruitment of endogenous endothelial cells via the paracrine activity of MSCs to promote the formation and extension of the vascular network within the niche. Diluted supernatants were used to avoid confounding factors associated with cell proliferation. Results demonstrated that the supernatant from ETV2-DPSCs facilitated wound healing, an effect attenuated by α-KG conditioned medium and partially rescued by IOX4 conditioned medium (Fig. 5D–H). Additionally, no significant impact was present on HUVEC proliferation across all groups (Fig. 5E), even when α-KG and IOX4 concentrations increased by a factor of 50 (Fig. S1E, F). Furthermore, α-KG exerted an impact on HIF-1 signaling in HUVECs. The ETV2 and IOX4 groups exhibited PHD2 downregulation, and HIF-1α and endothelial cell marker VE-Cadherin upregulation, while the NC and α-KG group displayed an opposite trend (Fig. 5F).

To further substantiate the impact of α-KG on angiogenesis, a matrigel plug assay was conducted in the armpit of nude mice. Matrigel plug assay is a well-established method for assessing functional angiogenesis in vivo [39]. After 7 d post-surgery, the size of resected matrigel plugs was significantly reduced in the α-KG group compared to the ETV2 group. Pharmacological intervention with IOX4 restored the tissue size (Fig. 5I). Immunofluorescence analysis demonstrated a trend consistent with the tissue size data, quantifying the proportion of the neovascular area (Fig. 5J). These findings collectively provide robust evidence to support the notion that ETV2-DPSCs promote local endothelial cell migration and the formation of vascular networks by reducing α-KG levels (Fig. 5K).

3.6. Characterization of HA/CS-MS

The fabrication process for HA/CS-MS using microfluidic technology is depicted in Fig. 6A. The process initiated with the use of an HA/CS acetic acid solution as the aqueous phase, which formed droplets through the shear force generated by the oil phase. These aqueous droplets were enveloped in the oil phase and subsequently released into an alkaline solution. As the pH of the solution changed from slightly acidic to neutral, the chitosan solution underwent rapid sol-gel transformation. This transformation results in hydroxyapatite encapsulation, forming microspheres [40].

By maintaining precise control over the flow ratio of the oil phase to the water phase, typically set at 20, the average diameter of the microspheres can be consistently maintained within the range of 150–210 μm (Fig. 6G) [41]. Further examination of the HA/CS-MS using SEM revealed that these microspheres were characterized by a uniform nanoscale fiber network (Fig. 6B). This intricate structure closely resembles the physical architecture of natural bone extracellular matrix. Previous studies have demonstrated the advantages of biomaterials featuring ECM-like nanofiber structures, including their ability to offer numerous focal adhesion sites, guide cell migration, and influence cell differentiation. Consequently, biomaterials that incorporate ECM-like nanofiber structures are expected to effectively support and regulate cell behavior and lineage fate, thereby promoting novel tissue formation.

Under bright-field microscopy, the microspheres exhibited a spherical shape with a uniform texture, smooth boundaries, and a high degree of monodispersity. When the DPSCs were incubated with these microspheres, they effectively adhered to and interconnected with the microspheres, forming complexes (Fig. 6C). Through X-ray diffraction analysis, we confirmed that the diffraction peaks of MS aligned with the standard peaks for HA and CS (Fig. 6D). Complemented by thermogravimetric analysis, it was established that MS consists of 44.567% hydroxyapatite and 55.433% chitosan (Fig. 6E). Energy dispersive spectrometer analysis demonstrated a homogeneous distribution of Ca and P elements representing hydroxyapatite and N elements representing chitosan within the microspheres (Fig. S5A), resembling the

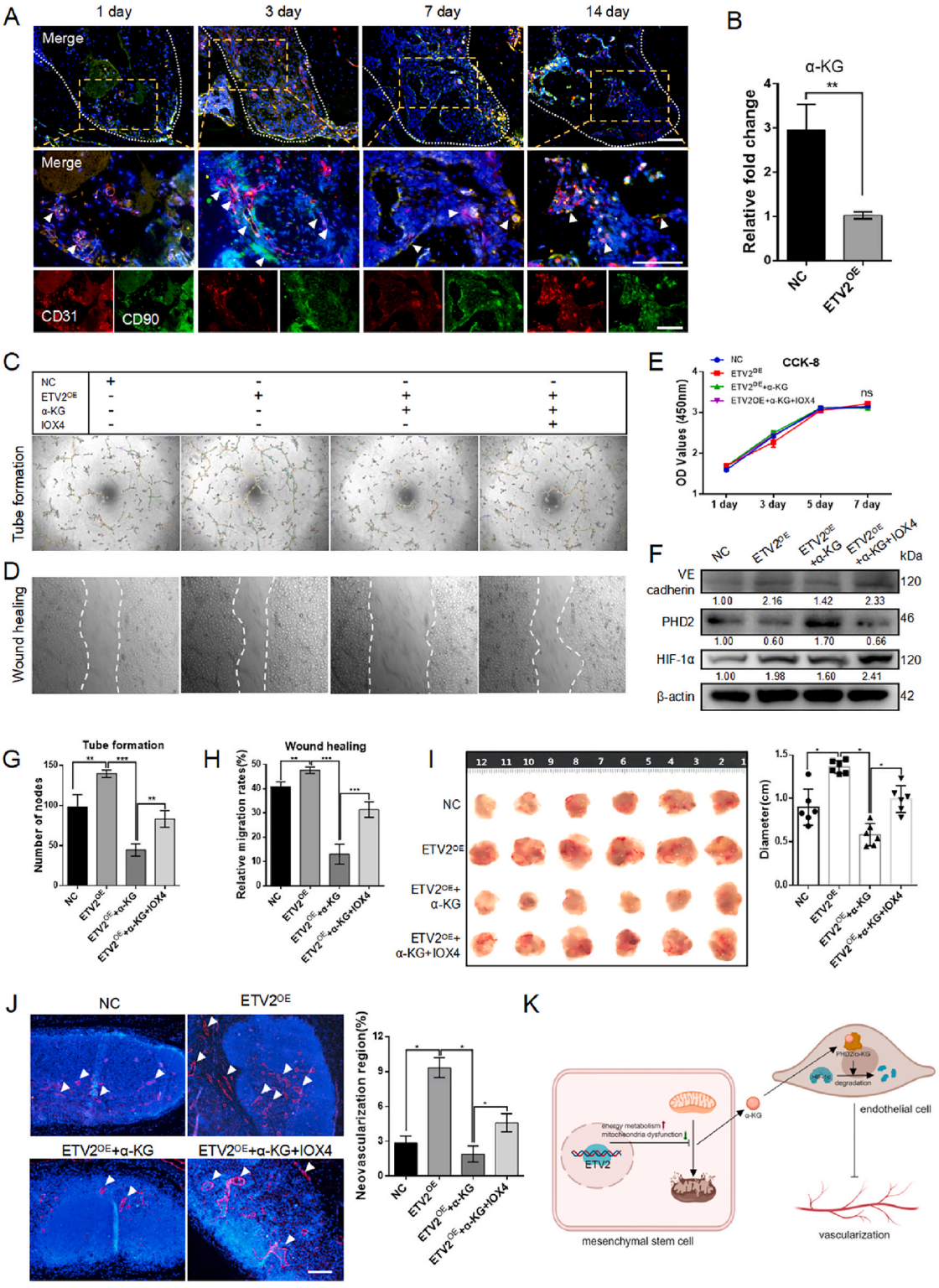

Fig. 5. Reduction of α-KG promotes angiogenesis (A) Representative images of immunofluorescence co-staining CD31 (red) and CD90 (green) in a mouse tooth extraction model. The white arrows indicate the close proximity of $CD31^{+}$ cells and $CD90^{+}$ cells. Scale bar: 100 μm (B) α-KG content in the culture supernatant of an equal number of NC-DPSCs and ETV2-DPSCs (C) Tube formation of HUVECs treated with an ETV2-conditioned medium, with or without the incorporation of α-KG or IOX4 (D) The wound healing assay conducted on HUVECs treated with ETV2-conditioned medium, both with and without α-KG or IOX4 incorporation (E) The CCK-8 assay of HUVECs treated by ETV2 conditioned medium with or without α-KG or IOX4 (F) The protein expression of PHD2, HIF-1α, and VE cadherin in HUVECs treated by ETV2 conditioned medium with or without α-KG or IOX4 (G, H) The statistical analysis of node numbers and relative migration rates in C and D (I) Macroscopic images and size analysis of resected Matrigel plug (J) Representative images and neovascularization region statistics of immunofluorescence labeling CD31 in Matrigel plug. The areas exhibiting positive staining are denoted by the white arrows. Scale bar: 100 μm (K) Schematic illustration of mechanism of vascularization (NC, negative control; OE, overexpression. Data are presented as the mean of >3 independent experiments ±SD. *P < 0.05, **P < 0.01, and ***P < 0.001).

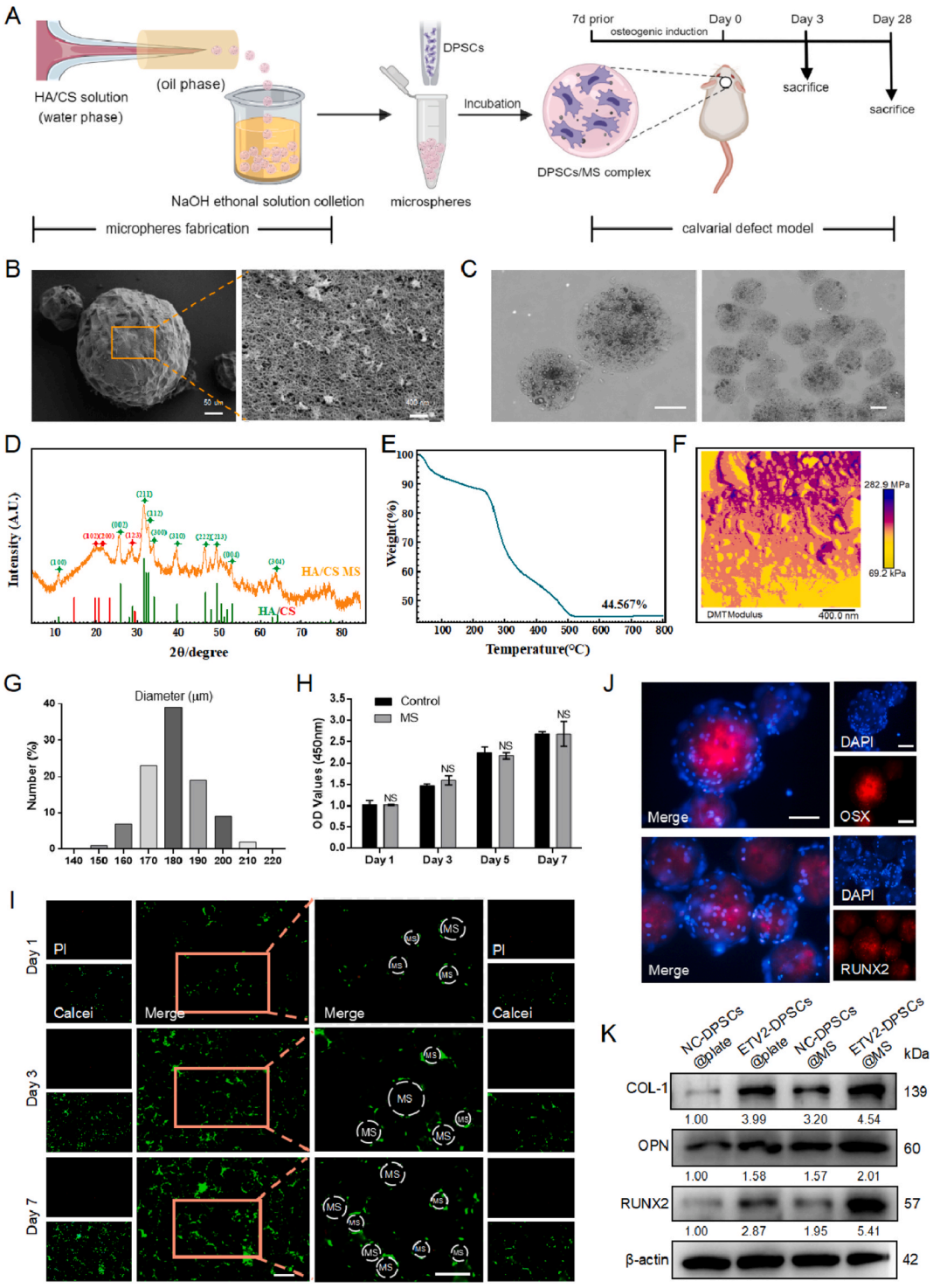

Fig. 6. ***In vitro*** **characterization of the biological properties of HA/CS MS** (A) Schematic diagram of the preparation and implantation of HA/CS MS into the rat critical-size bone defect. The flow chart is not drawn to scale. (B) SEM images of HA/CS MS (C) Morphological analysis of microspheres adhered with DPSCs under light microscope. Scale bar: 100 μm (D) X-ray diffraction spectrum of HA/CS MS (E) Thermodynamic analysis of HA/CS MS (F) Atomic force microscopy analysis of HA/CS MS (G) Particle size analysis of HA/CS MS (H) CCK-8 assay of microspheres incubated with DPSCs after 1, 3, 5, and 7 d (I) Representative images of Live-dead staining of DPSCs post incubation with microspheres for 1, 3, and 7 d. Live cells are green, dead cells are red, and the white dashed circle represents the microsphere. Scale bar: 200 μm (J) Representative images of immunofluorescence staining labeling RUNX2 and OSX in cells attached to MS post 7 d of osteogenic induction. Scale bar: 200 μm (K) The protein expression of COL-1, OPN, and RUNX2 after seven days of osteogenic induction in cells cultured on well plates or microsphere surfaces (MS, microsphere; NS, no significant difference; data are presented as the mean of >3 independent experiments ± SD).

distribution of hydroxyapatite crystals and collagen in the natural bone structure [42]. Atomic force microscopy analysis measured the elastic modulus of HA/CS MS as 147 ± 23.6 MPa (Fig. 6F).

To assess the biological properties of HA/CS-MS, the CCK-8 assay was employed to evaluate cell proliferation and cytotoxicity. The results demonstrated no significant differences in cell proliferation after 1, 3, 5, and 7 d of co-incubation with the material compared with that of the control (Fig. 6H). Live-dead staining verified that DPSCs adhering to the material displayed normal proliferation from days 1–7, with less number of dead cells observed, indicating the excellent biocompatibility of HA/CS-MS (Fig. 6I). Furthermore, to investigate whether the surfaces of the microspheres interfered with osteogenic differentiation, immunofluorescence staining for RUNX2 and OSX was conducted on adherent DPSCs after 7 d of osteogenic induction. The results demonstrated that adherent DPSCs exhibited normal RUNX2 and OSX expression, indicating their successful differentiation into the osteogenic lineage (Fig. 6J). Compared to well-plate cultures, qRT-PCR and Western blot results indicate that cells adhered to the microsphere surface exhibit higher expression levels of osteogenic genes at both mRNA and protein levels (Fig. 6K and Fig. S5B, C). These results imply that HA/CS MS contribute to an enhanced osteogenic differentiation of ETV2-DPSCs. In summary, the utilization of microfluidic technology allows for the precise and controlled fabrication of HA/CS-MS, featuring a biomimetic nanofiber structure and excellent bioactivity.

3.7. ETV2-DPSCs/MS accelerates the recovery of critical-size bone defects in vivo

The highly vascularized layers of the calvaria, as verified using high-resolution confocal images, encompass intricate networks of superficial reticulated skull vessels, penetrating vessels, and bone marrow sinusoids in the deeper layers of the skull [43]. Moreover, compared to the tooth extraction model, the calvarial defect model had fewer confounding factors affecting bone regeneration. Therefore, the critical-size calvarial defect model serves as a suitable platform for studying vascularized bone regeneration and has been extensively employed in numerous studies to assess the osteogenic and angiogenic properties of scaffold materials [44,45]. To evaluate the therapeutic effects of ETV2 on vascularized bone regeneration, we pre-differentiated a complex composed of microspheres loaded with transfected DPSCs for 7 d *in vitro*, ensuring osteogenic lineage commitment, and subsequently implanted it into a rat calvarial defect model (Fig. 6A).

To evaluate the in vivo safety of the composite, we initially performed inflammatory marker testing three days after material implantation. ELISA results indicated no significant differences in IL-6 and TNF-α levels among the groups compared to the control group (Fig. S6A). Following four weeks of material implantation, macroscopic images and H&E staining of vital organs revealed no apparent changes in morphology and structure (Fig. S6B, C).

Micro-CT is an exceptionally non-invasive method for quantitative assessment of bone tissue healing. Post four weeks, we conducted a three-dimensional reconstruction to evaluate the recovery of bone defects using micro-CT. The initial defect area with 5 mm diameter is indicated by an orange circle. From the reconstructed calvarial images, it is evident that the ETV2-DPSCs/MS group exhibited greater mineralized bone accumulation and the highest bone repair efficiency compared with those of the other groups, as observed in both the sagittal, top, and bottom views (Fig. 7A). In all the groups, a trend of defect repair was observed progressing from the periphery to the center. The ETV2 group displayed bone connections extending from the complex to the periphery, resulting in the formation of a continuously larger bone. Conversely, only sporadic bone regeneration was observed at the edges of the defect in the Blank and MS groups (Fig. 7A), indicating that neither the intrinsic self-healing capacity nor the microspheres alone could effectively repair critical-size bone defects (see Fig. 8).

In addition to the qualitative findings, quantitative analysis of bone microparameters revealed significant differences. The ETV2-DPSCs/MS group had a mean percentage of BS/TV of 3.91/mm ± 0.50/mm, which was 2.3 times greater than the MS group (Fig. 7B). Furthermore, the ETV2-DPSCs/MS group exhibited the highest values for BV/TV at 16.43% ± 1.05% and BMD at 0.90 g/m^3 ± 0.01 g/m^3, signifying bone regeneration with greater volume and intensity (Fig. 7B). Trabeculae are essential for supporting hematopoietic functions in the bone marrow cavity and play a crucial role in bone regeneration. The ETV2-DPSCs/MS group displayed a higher Tb. Th (Fig. 7B), indicating a more significant anabolic effect than bone catabolism [18].

Histological evaluation supported these radiological findings. In the blank group, H&E staining revealed that the defect area was covered with a thin, soft tissue, and almost no novel bone formation was observed around the microspheres in the MS group. In the NC-DPSCs/MS group, some bone formation occurred around the microspheres; however, was separated by fibrous tissue. Although the incorporation of DPSCs improved MS osteogenic potential to a certain extent, the prevalence of fibrous tissue in the defective area indicated insufficient osteoinductivity. Conversely, the ETV2-DPSCs/MS group displayed a substantial amount of novel bone around the microspheres with bone bridge formation. Importantly, the functional blood vessels were uniformly interspersed in the novel bone tissue (Fig. 7C). Similarly, Masson's trichrome staining revealed a higher amount of red-stained collagen around the microspheres in the ETV2-DPSCs/MS group than that in the other groups, indicating more mature novel bone formation (Fig. S7A).

To ascertain whether ETV2-DPSCs/MS promoted the rapid formation of a vascular network and osteogenesis by stabilizing hypoxic signals in a rat critical-size calvarial defect model, specimens were collected 3 d post-surgery. Immunofluorescence staining was conducted for the osteogenic makers, vascular marker, and HIF-1α. Compared to the MS and NC-DPSCs groups, the ETV2-DPSCs/MS group exhibited highest percentage of $RUNX2^+$ cells (Fig. 7D–H) and OSX^+ cells (Fig. S7B, E). CD31 immunofluorescence revealed a larger number of neovasculatures around the microspheres in the ETV2-DPSCs/MS group (Fig. 7E–I), suggesting that ETV2-DPSCs created a unique pro-angiogenesis niche. Furthermore, the ETV2-DPSCs/MS group exhibited rapid activation of the HIF-1 signaling pathway with high expression of HIF-1α (Fig. 7F–J) and inhibition of PHD2 (Fig. S7C, D).

To further validate osteogenesis at four weeks post-surgery, specific osteoblast markers Collagen I and OPN, were detected through immunofluorescence staining. A larger area of positive staining for OPN and Collagen I was observed (Fig. 7G–K, L), indicating the enhanced osteogenic activity of ETV2-DPSCs. Moreover, the positively stained cells were predominantly located at the edges of the microspheres and novel bone, suggesting that the transplanted DPSCs survived and differentiated into osteoblast lineage cells, contributing to novel bone deposition in the osteoblast niche. In general, our results indicate that ETV2-DPSCs/MS have a beneficial therapeutic effect on the rapid regeneration of vascularized bone in vivo.

4. Discussion

Emerging evidence has demonstrated that metabolic reprogramming is a significant factor in promoting osteoblast differentiation, independent of diverse signaling pathways and gene expressions [46]. Osteoblast-related cells are known for their energy-intensive metabolic activities and previous studies have highlighted the decisive role of energy metabolism in the antagonistic processes of osteogenic and lipogenic differentiation [10]. Metabolic decline caused by mitochondrial structural damage plays a crucial role in stem cell dysfunction associated with diseases, including bone aging, osteoporosis, rheumatoid arthritis, and osteoarthritis [47–49]. Targeted stem cell-based metabolic modulation demonstrates promise in alleviating these pathologies and achieving bone regeneration [50]. In this study, we observed that ETV2 is a key metabolic reprogramming transcription

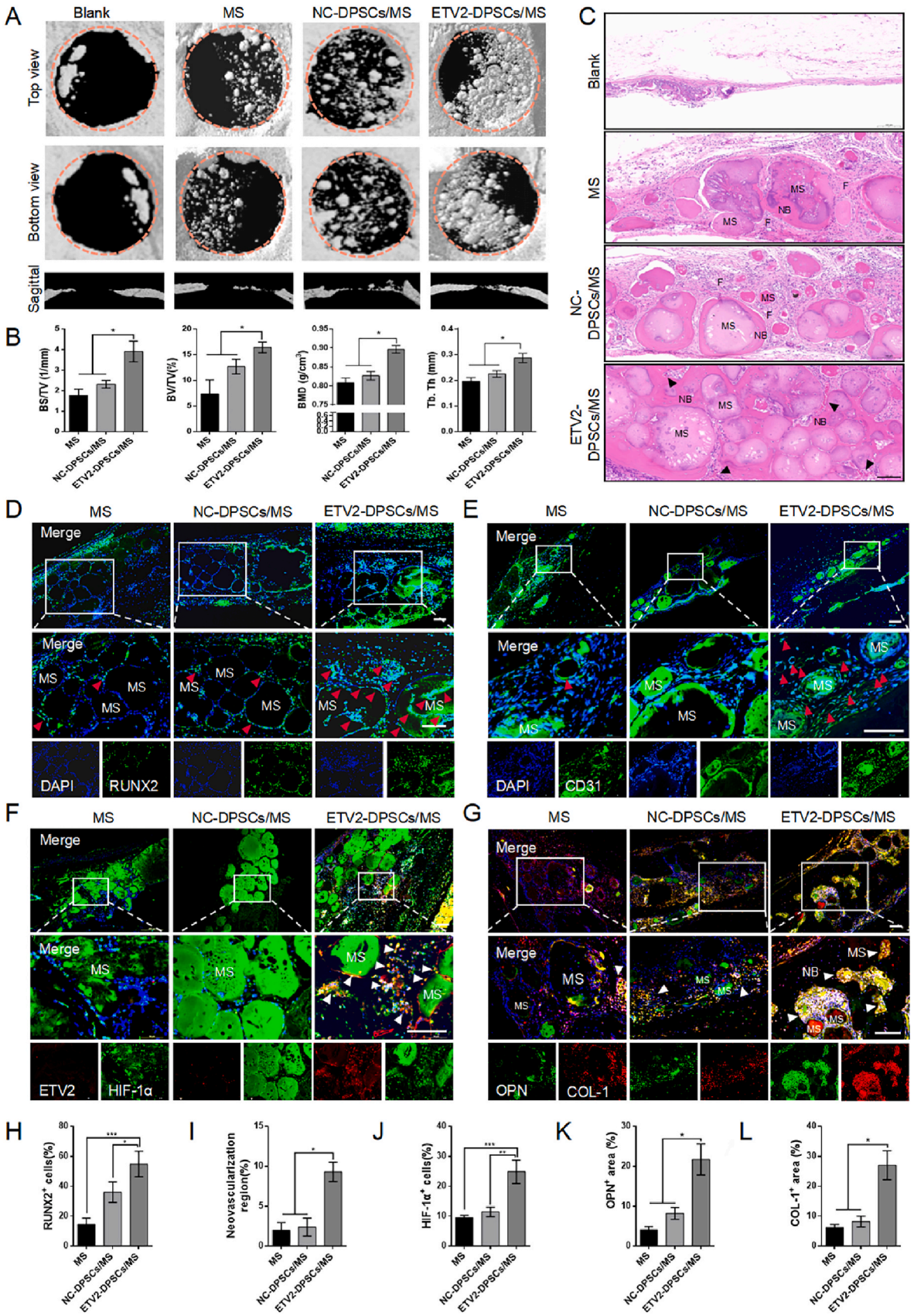

(caption on next page)

Fig. 7. ETV2-DPSCs/MS accelerate recovery of rat critical-size bone defect by rapid activation of HIF-1 signaling (A) Representative images of the three-dimensional reconstruction of rat calvarial defects using micro-CT at four weeks post-surgery. The orange circle outlines the 5 mm-diameter initial defect range. (B) Quantitative analyses of BMD, BV/TV, BS/TV, and Tb.Th (C) H&E staining of the defect area. The black arrow indicates neovasculars. Scale bar: 200 μm (D) Representative images of immunofluorescence labeling RUNX2 in tissue sections of defect area at 3 d post-modeling. Red arrows indicate $RUNX2^{+}$ cells. Scale bar: 200 μm (E) Representative images of immunofluorescence labeling CD31 in tissue sections of defect area at 3 d post-modeling. Red arrows indicate novel blood vessels. Scale bar: 200 μm (F) Representative images of immunofluorescence co-staining ETV2 (red) and HIF-1α (green) in tissue sections of defect area at 3 d post-modeling. Scale bar: 200 μm (G) Representative images of immunofluorescence co-staining OPN (green) and Collagen-1 (red) in tissue sections of defect area at four weeks post-modeling. Scale bar: 200 μm (H–L) Quantification of the proportion of $RUNX2^{+}$ cells, neovascularization region, $HIF\text{-}1\alpha^{+}$ cells, OPN^{+} area, and $COL\text{-}1^{+}$ area. (MS, microsphere; NB, novel bone; F, fibrous tissue; and NC, negative control. Data are presented as the mean of >3 independent experiments ±SD. *P < 0.05, **P < 0.01, and ***P < 0.001).

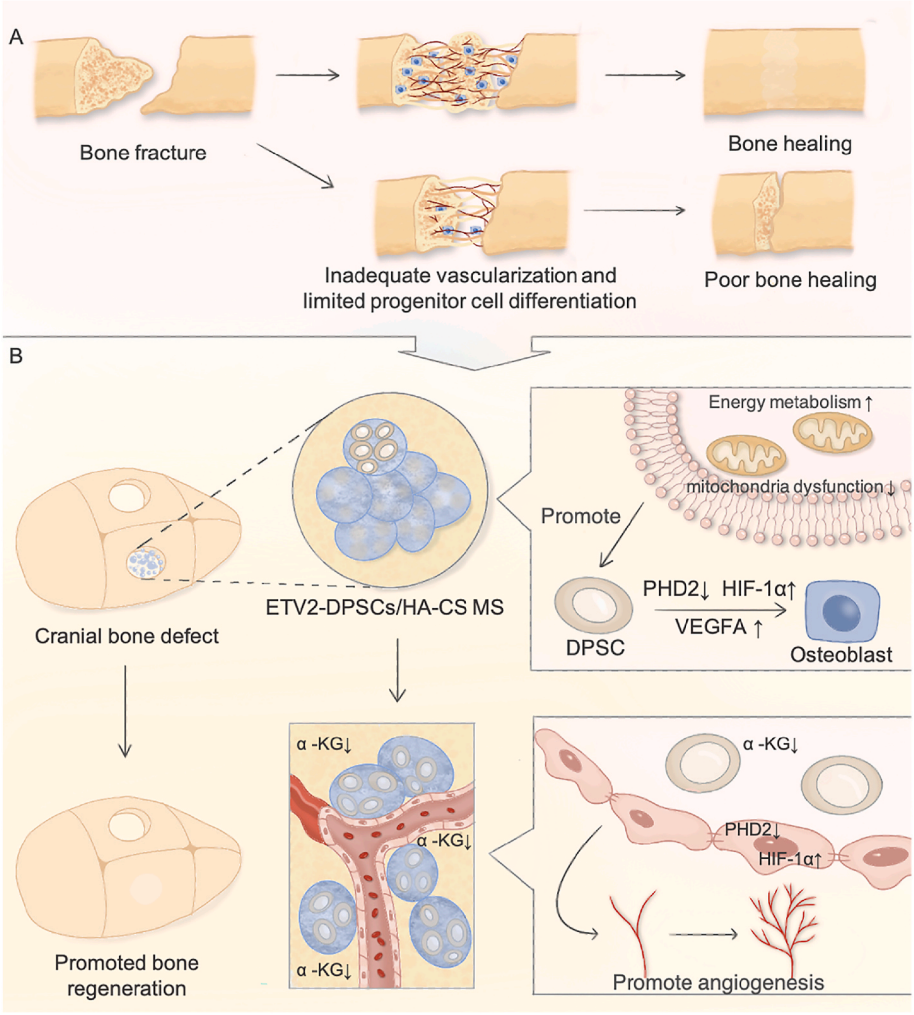

Fig. 8. This schematic illustrates the promoting effect of ETV2-DPSCs/MS on vascularized bone regeneration by local hypoxia signal homeostasis and energy metabolism reprogramming.

factor. We unveiled a substantial boost in energy metabolic orchestrated by ETV2 through two distinct mechanisms: the augmentation of anaerobic glycolysis driven by HIF-1α and the enhancement of aerobic respiration achieved by safeguarding mitochondrial function. These results jointly formed the basis for the proosteogenic effect of ETV2.

HIF-1α is a potential osteogenesis and angiogenesis regulator, yet the specific molecular mechanism and activation mode underlying its function have remained obscure [15]. Deferoxamine (DFO), a classical HIF-1α activator, can inhibit PHD2 by competitively binding Fe^{2+} [51]. Several studies have demonstrated that strategies combining materials with DFO coordinate the synergistic development of bone and vascular regeneration [18,52]. However, the potential drug toxicity has raised concern. Here, we demonstrated that ETV2 initiates HIF-1 signaling by suppressing PHD2 transcription and promoting osteogenic differentiation through endogenous VEGFA expression. The unique microenvironment with reduced α-KG from ETV2-DPSCs activates the hypoxia signaling pathway in endothelial cells by PHD2 dysfunction, consequently triggering migration-induced angiogenesis. These findings suggest that ETV2 acts as an effective factor coupling of osteogenesis and angiogenesis by regulating the HIF-1 signaling, showcasing potent potential for vascularized bone regeneration. The mammalian skeletal system is intricately innervated by both neural and vascular networks. Collaboration between the nervous and vascular systems plays a crucial role in shaping the microenvironment for bone tissue development and regeneration [53]. DPSCs have been verified to possess the potential to differentiate into neuronal cells [54]. Given the high metabolic activity required for neural cell development, the possibility whether ETV2 can mediate the differentiation of stem cells into both osteogenic and

neuronal lineages and induce vascular reconstruction by modulating the local microenvironment, and thus achieve comprehensive functionalized bone tissue regeneration, will be further investigated in future studies.

Scaffold materials are critical for optimizing bone tissue engineering. The microsphere scaffold with biomimicking nanostructure enable support excellent cell binding, metabolic activity, specific differentiations, and reconstruction of the stem cell niche [21,22]. To take complete advantage of the metabolic activity and microenvironmental regulation of ETV2, we fabricated HA/CS MS using microfluidic technology. The chemical structure and crystalline state of nano-hydroxyapatite closely resemble those of natural hydroxyapatite, and chitosan replicates the structural characteristics of the extracellular matrix of bone [40,55]. These two components simulate the inorganic and organic compositions of natural bone and exhibit excellent histocompatibility and good degradability [23,56]. Moreover, in comparison to conventional culture on well plates, the distinctive composition and nanoscale surface of the microspheres further enhanced the osteogenic differentiation of stem cells. This underscores their potential as excellent carriers for bone tissue engineering. Ultimately, in a challenging critical-size bone defect model, the synergistic combination of ETV2-DPSCs and HA/CS MS facilitated the rapid regeneration of vascularized bone, demonstrating outstanding in vivo safety. In the future, microsphere composites could also serve as multifunctional scaffold supplements combined with bone-conductive scaffolds with macroporosity to enhance bone regeneration [57].

5. Conclusion

Herein, we found that ETV2 functions as a key transcription factor that promotes energy metabolism reprogramming and osteogenesis and angiogenesis coupling. Specifically, ETV2 induces the stabilization and functional activation of HIF-1α in DPSCs through targeted PHD2 inhibition and the promotion of ERK1/2 phosphorylation and enhances osteogenic differentiation of DPSCs by ETV2-PHD2-HIF1A-VEGFA axis. ETV2 improved both aerobic respiration and anaerobic glycolysis, meeting the prerequisites for effective differentiation. Alternatively, the decrease in α-KG levels from ETV2-DPSCs initiates hypoxic signaling in peripheral endothelial cells, leading to enhanced migration and vessel formation. Additionally, HA/CS MS were engineered for efficient cell delivery in vascularized bone tissue engineering. The HA/CS MS not only possesses a biomimetic nanostructure but also contributes to the reconstruction of the in situ niche and further enhanced the osteogenic differentiation of DPSCs. Most significantly, HA/CS MS loaded with ETV2-overexpressing DPSCs demonstrated a remarkable potential for vascularized bone regeneration in critical-size rat bone defects. In summary, ETV2 equips DPSCs with the capacity to enhance their energy metabolism and orchestrate osteogenesis and angiogenesis. The combination of ETV2-DPSCs with HA/CS MS offers promising prospects for the clinical repair of critical bone defects.

Funding

This work was supported by the National Natural Science Foundation of China (grants 82301039), the Natural Science Foundation of the Anhui Higher Education Institutions of China (grant 2022AH050758), Anhui Institute of Translational Medicine, Natural Sciences (grant 2022zhyx-C87), National Natural Science Foundation of China (82170951), Beijing Municipal Natural Science Foundation (7222079).

CRediT authorship contribution statement

HaoRan Du: Writing – review & editing, Writing – original draft, Data curation, Conceptualization. **Bang Li:** Writing – review & editing, Data curation, Conceptualization. **Rui Yu:** Data curation. **Xiaoxuan Lu:** Data curation. **ChengLin Li:** Data curation. **HuiHui Zhang:** Data curation. **Fan Yang:** Data curation. **RongQuan Zhao:** Data curation. **WeiMin Bao:** Data curation. **Xuan Yin:** Data curation. **YuanYin Wang:** Conceptualization. **Jian Zhou:** Conceptualization. **Jianguang Xu:** Conceptualization.

Declaration of competing interest

The authors declare that they have no known competing financial interests or personal relationships that could have appeared to influence the work reported in this paper.

Appendix A. Supplementary data

Supplementary data to this article can be found online at https://doi.org/10.1016/j.bioactmat.2024.02.014.

References

[1] R. Dimitriou, E. Jones, D. McGonagle, P.V. Giannoudis, Bone regeneration: current concepts and future directions, BMC Med. 9 (2011) 66.
[2] V. Campana, G. Milano, E. Pagano, M. Barba, C. Cicione, G. Salonna, W. Lattanzi, G. Logroscino, Bone substitutes in orthopaedic surgery: from basic science to clinical practice, J. Mater. Sci. Mater. Med. 25 (2014) 2445–2461.
[3] D.J. Hak, D. Fitzpatrick, J.A. Bishop, J.L. Marsh, S. Tilp, R. Schnettler, H. Simpson, V. Alt, Delayed union and nonunions: epidemiology, clinical issues, and financial aspects, Injury 45 (Suppl 2) (2014) S3–S7.
[4] B. Wildemann, A. Ignatius, F. Leung, L.A. Taitsman, R.M. Smith, R. Pesántez, M. J. Stoddart, R.G. Richards, J.B. Jupiter, Non-union bone fractures, Nat. Rev. Dis. Prim. 7 (2021) 57.
[5] H. Eftekhari, A. Jahandideh, A. Asghari, A. Akbarzadeh, S. Hesaraki, Assessment of polycaprolacton (PCL) nanocomposite scaffold compared with hydroxyapatite (HA) on healing of segmental femur bone defect in rabbits, Artif. Cell Nanomed. Biotechnol. 45 (2017) 961–968.
[6] E. Nyberg, A. Rindone, A. Dorafshar, W.L. Grayson, Comparison of 3D-printed poly-ε-caprolactone scaffolds functionalized with tricalcium phosphate, hydroxyapatite, bio-oss, or decellularized bone matrix, Tissue Eng. 23 (2017) 503–514.
[7] H.N. Chia, B.M. Wu, Recent advances in 3D printing of biomaterials, J. Biol. Eng. 9 (2015) 4.
[8] M.M. Stevens, Biomaterials for bone tissue engineering, Mater. Today 11 (2008) 18–25.
[9] N. Dirckx, M.C. Moorer, T.L. Clemens, R.C. Riddle, The role of osteoblasts in energy homeostasis, Nat. Rev. Endocrinol. 15 (2019) 651–665.
[10] H. Zhang, R. Xu, B. Li, Z. Xin, Z. Ling, W. Zhu, X. Li, P. Zhang, Y. Fu, J. Chen, L. Liu, J. Cheng, H. Jiang, LncRNA NEAT1 controls the lineage fates of BMSCs during skeletal aging by impairing mitochondrial function and pluripotency maintenance, Cell Death Differ. 29 (2022) 351–365.
[11] A.R. Guntur, P.T. Le, C.R. Farber, C.J. Rosen, Bioenergetics during calvarial osteoblast differentiation reflect strain differences in bone mass, Endocrinology 155 (2014) 1589–1595.
[12] C.T. Chen, Y.R. Shih, T.K. Kuo, O.K. Lee, Y.H. Wei, Coordinated changes of mitochondrial biogenesis and antioxidant enzymes during osteogenic differentiation of human mesenchymal stem cells, Stem cells (Dayton, Ohio) 26 (2008) 960–968.
[13] J. Maity, M. Deb, C. Greene, H. Das, KLF2 regulates dental pulp-derived stem cell differentiation through the induction of mitophagy and altering mitochondrial metabolism, Redox Biol. 36 (2020) 101622.
[14] S.W. Teh, A.E. Koh, J.B. Tong, X. Wu, A.V. Samrot, S. Rampal, P.L. Mok, S. K. Subbiah, Hypoxia in bone and oxygen releasing biomaterials in fracture treatments using mesenchymal stem cell therapy: a review, Front. Cell Dev. Biol. 9 (2021) 634131.
[15] J. Tao, R. Miao, G. Liu, X. Qiu, B. Yang, X. Tan, L. Liu, J. Long, W. Tang, W. Jing, Spatiotemporal correlation between HIF-1α and bone regeneration, in: FASEB Journal : Official Publication of the Federation of American Societies for Experimental Biology, vol. 36, 2022 e22520.
[16] A.P. Kusumbe, S.K. Ramasamy, R.H. Adams, Coupling of angiogenesis and osteogenesis by a specific vessel subtype in bone, Nature 507 (2014) 323–328.
[17] X. Zheng, X. Zhang, Y. Wang, Y. Liu, Y. Pan, Y. Li, M. Ji, X. Zhao, S. Huang, Q. Yao, Hypoxia-mimicking 3D bioglass-nanoclay scaffolds promote endogenous bone regeneration, Bioact. Mater. 6 (2021) 3485–3495.
[18] J. Zhang, D. Tong, H. Song, R. Ruan, Y. Sun, Y. Lin, J. Wang, L. Hou, J. Dai, J. Ding, H. Yang, Osteoimmunity-regulating biomimetically hierarchical scaffold for augmented bone regeneration, Adv. Mater. 34 (2022) e2202044.
[19] X. Han, M. Sun, B. Chen, Q. Saiding, J. Zhang, H. Song, L. Deng, P. Wang, W. Gong, W. Cui, Lotus seedpod-inspired internal vascularized 3D printed scaffold for bone tissue repair, Bioact. Mater. 6 (2021) 1639–1652.
[20] K. Choi, ETS transcription factor ETV2/ER71/Etsrp in haematopoietic regeneration, Curr. Opin. Hematol. 25 (2018) 253–258.
[21] N. Sarviya, S.M. Basu, V. Induvahi, J. Giri, Laponite-Gelatin nanofibrous microsphere promoting human dental follicle stem cells attachment and osteogenic

differentiation for noninvasive stem cell transplantation, Macromol. Biosci. 23 (2023) e2200347.
[22] N. Sarviya, S.M. Basu, R. Mani, M. Chauhan, P. Kingshott, J. Giri, Biomimicking nanofibrous gelatin microspheres recreating the stem cell niche for their ex-vivo expansion and in-vivo like differentiation for injectable stem cell transplantation, Biomater. Adv. 139 (2022) 212981.
[23] R. Ding, Y. Liu, D. Cheng, G. Yang, W. Wu, H. Du, X. Jin, Y. Chen, Y. Wang, B. C. Heng, Q. Yang, J. Xu, A novel gene-activated matrix composed of PEI/plasmid-BMP2 complexes and hydroxyapatite/chitosan-microspheres promotes bone regeneration, Nano Res. 15 (2022) 6348–6360.
[24] X. Zhou, J. Liu, Y. Zheng, Z. Zhang, Y. Wu, W. Yang, J. Liu, Y. Huang, Y. Yi, Z. Zhao, H. Xiao, X. Mo, J. Wang, SM22α-lineage niche cells regulate intramembranous bone regeneration via PDGFRβ-triggered hydrogen sulfide production, Cell Rep. 39 (2022) 110750.
[25] M.G. Araújo, C.O. Silva, M. Misawa, F. Sukekava, Alveolar socket healing: what can we learn? Periodontol. 2000 68 (2015) 122–134.
[26] M. Ponzetti, N. Rucci, Osteoblast differentiation and signaling: established concepts and emerging topics, Int. J. Mol. Sci. (2021) 22.
[27] R.J. Appelhoff, Y.M. Tian, R.R. Raval, H. Turley, A.L. Harris, C.W. Pugh, P. J. Ratcliffe, J.M. Gleadle, Differential function of the prolyl hydroxylases PHD1, PHD2, and PHD3 in the regulation of hypoxia-inducible factor, J. Biol. Chem. 279 (2004) 38458–38465.
[28] J. Li, H. Du, X. Ji, Y. Chen, Y. Li, B.C. Heng, J. Xu, ETV2 promotes osteogenic differentiation of human dental pulp stem cells through the ERK/MAPK and PI3K-Akt signaling pathways, Stem Cell Res. Ther. 13 (2022) 495.
[29] X. Duan, S.R. Bradbury, B.R. Olsen, A.D. Berendsen, VEGF stimulates intramembranous bone formation during craniofacial skeletal development, Matrix Biol. 52–54 (2016) 127–140.
[30] C. Yu, R. Sautchuk, J. Martinez, R.A. Eliseev, Mitochondrial permeability transition regulator, cyclophilin D, is transcriptionally activated by C/EBP during adipogenesis, J. Biol. Chem. 299 (2023) 105458.
[31] J.K. Salabei, A.A. Gibb, B.G. Hill, Comprehensive measurement of respiratory activity in permeabilized cells using extracellular flux analysis, Nat. Protoc. 9 (2014) 421–438.
[32] L.C. Shum, N.S. White, B.N. Mills, K.L. Bentley, R.A. Eliseev, Energy metabolism in mesenchymal stem cells during osteogenic differentiation, Stem Cell. Dev. 25 (2016) 114–122.
[33] C. Yong, G.D. Stewart, C. Frezza, Oncometabolites in renal cancer, Nat. Rev. Nephrol. 16 (2020) 156–172.
[34] A.V. Kozhukhar, I.M. Yasinska, V.V. Sumbayev, Nitric oxide inhibits HIF-1alpha protein accumulation under hypoxic conditions: implication of 2-oxoglutarate and iron, Biochimie 88 (2006) 411–418.
[35] Y.A. Wen, X. Xiong, T. Scott, A.T. Li, C. Wang, H.L. Weiss, L. Tan, E. Bradford, T.W. M. Fan, N.S. Chandel, T.A. Barrett, T. Gao, The mitochondrial retrograde signaling regulates Wnt signaling to promote tumorigenesis in colon cancer, Cell Death Differ. 26 (2019) 1955–1969.
[36] L.M. Calvi, G.B. Adams, K.W. Weibrecht, J.M. Weber, D.P. Olson, M.C. Knight, R. P. Martin, E. Schipani, P. Divieti, F.R. Bringhurst, L.A. Milner, H.M. Kronenberg, D. T. Scadden, Osteoblastic cells regulate the haematopoietic stem cell niche, Nature 425 (2003) 841–846.
[37] Celso C. Lo, H.E. Fleming, J.W. Wu, C.X. Zhao, S. Miake-Lye, J. Fujisaki, D. Côté, D. W. Rowe, C.P. Lin, D.T. Scadden, Live-animal tracking of individual haematopoietic stem/progenitor cells in their niche, Nature 457 (2009) 92–96.
[38] C. Nombela-Arrieta, G. Pivarnik, B. Winkel, K.J. Canty, B. Harley, J.E. Mahoney, S. Y. Park, J. Lu, A. Protopopov, L.E. Silberstein, Quantitative imaging of haematopoietic stem and progenitor cell localization and hypoxic status in the bone marrow microenvironment, Nat. Cell Biol. 15 (2013) 533–543.
[39] P. Kastana, F.T. Zahra, D. Ntenekou, S. Katraki-Pavlou, D. Beis, M.S. Lionakis, C. M. Mikelis, E. Papadimitriou, Matrigel plug assay for in vivo evaluation of angiogenesis, Methods Mol. Biol. 1952 (2019) 219–232.
[40] B. Chang, N. Ahuja, C. Ma, X. Liu, Injectable scaffolds: preparation and application in dental and craniofacial regeneration, Mater. Sci. Eng. R Rep. 111 (2017) 1–26.
[41] S.L. Xin Zhao, Yildirimer Lara, Hong Zhao, Ruihua Ding, Huanan Wang, Wenguo Cui, David Weitz, Injectable stem cell-laden photocrosslinkable microspheres fabricated using microfluidics for rapid generation of osteogenic tissue constructs, Adv. Funct. Mater. 26 (2016) 2809–2819.
[42] D. Lopes, C. Martins-Cruz, M.B. Oliveira, J.F. Mano, Bone physiology as inspiration for tissue regenerative therapies, Biomaterials 185 (2018) 240–275.
[43] W. Li, Y.H. Liu, H. Estrada, J. Rebling, M. Reiss, S. Galli, C. Nombela-Arrieta, D. Razansky, Tracking strain-specific morphogenesis and angiogenesis of murine calvaria with large-scale optoacoustic and ultrasound microscopy, in: Journal of Bone and Mineral Research : the Official Journal of the American Society for Bone and Mineral Research, vol. 37, 2022, pp. 1032–1043.
[44] D. Wu, X. Chang, J. Tian, L. Kang, Y. Wu, J. Liu, X. Wu, Y. Huang, B. Gao, H. Wang, G. Qiu, Z. Wu, Bone mesenchymal stem cells stimulation by magnetic nanoparticles and a static magnetic field: release of exosomal miR-1260a improves osteogenesis and angiogenesis, J. Nanobiotechnol. 19 (2021) 209.
[45] Y. Chen, Y. Wu, L. Guo, S. Yuan, J. Sun, K. Zhao, J. Wang, R. An, Exosomal Lnc NEAT1 from endothelial cells promote bone regeneration by regulating macrophage polarization via DDX3X/NLRP3 axis, J. Nanobiotechnol. 21 (2023) 98.
[46] R.K. Srivastava, L. Sapra, P.K. Mishra, Osteometabolism: metabolic alterations in bone pathologies, Cells (2022) 11.
[47] T. Miyazaki, M. Iwasawa, T. Nakashima, S. Mori, K. Shigemoto, H. Nakamura, H. Katagiri, H. Takayanagi, S. Tanaka, Intracellular and extracellular ATP coordinately regulate the inverse correlation between osteoclast survival and bone resorption, J. Biol. Chem. 287 (2012) 37808–37823.
[48] D. Chen, X. Cai, H. Ouyang, S. Yuan, X. Wang, L. Lin, Z. Chen, M. Huang, Increased eEF2K promotes glycolysis and aggressive behaviors of fibroblast-like synoviocytes in rheumatoid arthritis, J. Inflamm. Res. 15 (2022) 1729–1744.
[49] C.X. Zheng, B.D. Sui, X.Y. Qiu, C.H. Hu, Y. Jin, Mitochondrial regulation of stem cells in bone homeostasis, Trends Mol. Med. 26 (2020) 89–104.
[50] S. Lucas, Y. Omata, J. Hofmann, M. Böttcher, A. Iljazovic, K. Sarter, O. Albrecht, O. Schulz, B. Krishnacoumar, G. Krönke, M. Herrmann, D. Mougiakakos, T. Strowig, G. Schett, M.M. Zaiss, Short-chain fatty acids regulate systemic bone mass and protect from pathological bone loss, Nat. Commun. 9 (2018) 55.
[51] A.C. Farr, M.P. Xiong, Challenges and opportunities of deferoxamine delivery for treatment of alzheimer's disease, Parkinson's disease, and intracerebral hemorrhage, Mol. Pharm. 18 (2021) 593–609.
[52] Y. Li, J. Zhu, X. Zhang, Y. Li, S. Zhang, L. Yang, R. Li, Q. Wan, X. Pei, J. Chen, J. Wang, Drug-delivery nanoplatform with synergistic regulation of angiogenesis-osteogenesis coupling for promoting vascularized bone regeneration, ACS Appl. Mater. Interfaces 15 (2023) 17543–17561.
[53] Q.Q. Wan, W.P. Qin, Y.X. Ma, M.J. Shen, J. Li, Z.B. Zhang, J.H. Chen, F.R. Tay, L. N. Niu, K. Jiao, Crosstalk between bone and nerves within bone, Adv. Sci. 8 (2021) 2003390.
[54] V. Mayo, Y. Sawatari, C.Y. Huang, F. Garcia-Godoy, Neural crest-derived dental stem cells–where we are and where we are going, J. Dent. 42 (2014) 1043–1051.
[55] H. Zhou, J. Lee, Nanoscale hydroxyapatite particles for bone tissue engineering, Acta Biomater. 7 (2011) 2769–2781.
[56] P. Feng, P. Wu, C. Gao, Y. Yang, W. Guo, W. Yang, C. Shuai, A multimaterial scaffold with tunable properties: toward bone tissue repair, Adv. Sci. 5 (2018) 1700817.
[57] H.Y. Yang, L.N. Niu, J.L. Sun, X.Q. Huang, D.D. Pei, C. Huang, F.R. Tay, Biodegradable mesoporous delivery system for biomineralization precursors, Int. J. Nanomed. 12 (2017) 839–854.